Palaeogeography, Palaeoclimatology, Palaeoecology 686 (2026) 113551

Contents lists available at ScienceDirect

Palaeogeography, Palaeoclimatology, Palaeoecology

journal homepage: www.elsevier.com/locate/palaeo

Palaeoenvironmental reconstruction from Hulas Khera: Insights into mid-late Holocene hydroclimatic variability in the Central Ganga Plain☆

Arvind Tiwari [a,b,*], Binita Phartiyal [a,b,*], M.C. Manoj [a,b], Masud Kawsar [d], K. Prasanna [a,b], Rajveer Sharma [c], Pankaj Kumar [c], Anupam Sharma [a,b]

[a] Birbal Sahni Institute of Palaeosciences, 53-University Road, Lucknow, Uttar Pradesh 226007, India
[b] Academy of Scientific and Innovative Research, Ghaziabad, Uttar Pradesh 201002, India
[c] Inter-University Accelerator Centre, Aruna Asaf Ali Marg, New Delhi 110067, India
[d] Indian Institute of Tropical Meteorology, Dr Homi Bhabha Road, Pashan, Pune, Maharashtra 411008, India

ARTICLE INFO

Editor: Pradeep Srivastava

Keywords:
Central Ganga Plain
Palaeoclimate
Mineral magnetism
Textural analysis
Indian Summer Monsoon

ABSTRACT

This study from Hulas Khera, in the Central Ganga Plain, reconstructs past climatic conditions and lake-level fluctuations since ~6350 calibrated years BP. It integrates sediment textural analysis, mineral magnetism, elemental composition, and AMS radiocarbon dating. Variations in detrital input reflect catchment erosion associated with shifts in rainfall patterns, indicating precipitation as the primary driver of magnetic property changes. The C-M diagram indicates floodplain deposition, driven by suspension settling. Grain-size end-members EM1 and EM2 (mean sizes: 8.9 and 53 μm) in the fine to coarse silt domain are associated with surface runoff during periods of heightened seasonal precipitation, corresponding to intensified Indian Summer Monsoon activity around 5400 to 4600, 4000, 3300, 2000, and 800 cal yrs. BP. In contrast, EM3 and EM4 (mean sizes: 92 and 160 μm), within fine sand domain, are prominent during intervals of extended drought and monsoon minima around ~6300–5400, ~4300, ~3600, ~2800–2200, ~1800–900, and ~ 600–300 cal yrs. BP, coinciding with regional dry phases recorded in the Kanwar Lake record from the Central Ganga Plain, and reduced upwelling record of the Arabian Sea. Abrupt shifts in Indian Summer Monsoon (ISM) strength recorded correspond to known monsoon minima during the Little Ice Age and the Dark Age Cold Period, highlighting the sensitivity of regional hydrodynamics to mid- to late-Holocene monsoonal variability.

1. Introduction

The Indo-Gangetic Plain, situated within the Himalayan foreland basin, represents the world's largest fluvially controlled depositional system. It acts as a repository for sediment load received from the Himalayas to the north, supplemented by contributions from the Vindhyan highlands to the south (Srivastava et al., 2003a). Owing to its fertile soils, abundant water resources, and ecological diversity, the Ganga Basin has supported continuous human habitation since the Stone Age (Jha et al., 2024). As one of the most agriculturally productive regions of the Indian subcontinent, the Ganga Plain underpins a monsoon-dependent agrarian culture. Geomorphologically, the region is divided into three sectors: the Upper Ganga Plain, the Central Ganga Plain (CGP), and the Lower Ganga Plain, distinguished by their varying rates of subsidence and sediment accumulation. Among these, the CGP is the largest, occupying ~1.44 lakh km^2 between 81°47'E–87°50'E and 24°30'N–27°50'N. Considering the broad geographical extent of the CGP, stretching from east to west and north to south, the region exhibits a transitional climatic character. CGP is characterized by diverse geomorphic features, including fluvial channels, terraces, lakes, ponds, and swamps. The area is drained by the Ghaghara, Gandak, and Kosi rivers, as well as tributaries of the Ganga that originate in the Himalayas. These regions contain large alluvial fans of the Kosi and Gandak rivers, as well as several small alluvial fans (Sinha et al., 2005).

During the Late Quaternary, climatic fluctuations and associated base-level changes led to the development of the principal geomorphic surfaces of the Ganga Plain (Singh et al., 1997; Singh, 1996). The most prominent of these is the upland interfluve surface, an extensive remnant plain situated between active river channels. This surface is interspersed with numerous lakes and ponds, which act as sediment

☆ This article is part of a Special issue entitled: 'Afro Asian Monsoon' published in Palaeogeography, Palaeoclimatology, Palaeoecology.

* Corresponding authors at: Birbal Sahni Institute of Palaeosciences, 53-University Road, Lucknow, Uttar Pradesh 226007, India.
E-mail addresses: arvind.tiwari@bsip.res.in (A. Tiwari), binita_phartiyal@bsip.res.in (B. Phartiyal).

https://doi.org/10.1016/j.palaeo.2026.113551
Received 26 September 2025; Received in revised form 1 December 2025; Accepted 6 January 2026
Available online 9 January 2026

traps, preserving fine-grained deposits that would otherwise be transported downstream (Singh, 1996; Srivastava et al., 2003b). The sediments deposited within these lakes and ponds constitute high-resolution palaeoclimatic archives, preserving detailed and continuous records of Late Quaternary climate variability, including shifts in fluvial dynamics and monsoonal intensity (Singh et al., 2015), which are governed by regional and global climatic variations. These lakes and ponds have played a significant role in agricultural development since ancient times, supporting human settlements (Pokharia et al., 2017). Hence, the Ganga Plain in India is of significant scientific relevance to palaeoclimate studies due to its unique geological, geomorphological, and climatic characteristics.

The region's climate is influenced by monsoonal variability, which has historically shaped vegetation patterns, human settlement, and agricultural practices. The primary sources of freshwater in this region are the Indian Summer Monsoon, snowmelt from the Himalayan Mountains, and groundwater (Lutz et al., 2014). The strength, duration, and magnitude of the ISM are key factors responsible for shaping the societal, agricultural, and economic prosperity of the Ganga Basin. Monsoons have a bearing on the socio-economic fabric of South Asia, with abrupt shifts in ISM activity driving the rise and fall of ancient civilizations (Gupta et al., 2006; Thamban et al., 2007). ISM is a complex climatic system regulated by solar forcing (Agnihotri et al., 2002) and coupled ocean-atmosphere dynamics (Gupta et al., 2003; Phartiyal et al., 2024). ISM intensity is closely related to Intertropical Convergence Zone (ITCZ) shifts driven by Northern Hemisphere insolation variability (Fleitmann et al., 2003; Gadgil, 2018).

Most Holocene lake-based climatic records from the Indian subcontinent are limited by poor to moderate temporal resolution, stemming from weak chronological control or coarse sampling intervals. The few high-resolution studies available across different basins often show inconsistent centennial- to millennial-scale climate trends, likely reflecting spatial variations in precipitation patterns (Rawat et al., 2021). These limitations have hindered our understanding of the forcing mechanisms driving ISM variability on shorter time scales, particularly during the Holocene when rapid shifts in monsoon intensity had significant societal and environmental consequences (Kathayat et al., 2017). Monsoon variability has been extensively reconstructed from marine archives (Agnihotri et al., 2002; Gupta et al., 2003; Overpeck et al., 1996; Ponton et al., 2012; Staubwasser et al., 2002) and from terrestrial records (Dixit et al., 2014; Mishra et al., 2015; Prasad et al., 2014; Sinha et al., 2007; Srivastava et al., 2017).

Although the CGP has been the focus of many palaeoclimatic records (Chauhan et al., 2015; Kumar et al., 2022; Misra et al., 2020; Phartiyal et al., 2024; Saxena et al., 2015, Saxena et al., 2013; Sengupta et al., 2024; Sharma et al., 2004; Singh et al., 2015; Singh et al., 2022; Tripathi et al., 2017; Trivedi et al., 2019, Trivedi et al., 2013) which have provided valuable insights into Holocene climatic variability; however, most studies rely on a single-proxy approach characterized by coarse sampling resolution and chronological constraints, while only few multi-proxy based high-resolution studies supported strong chronology have been carried out. This highlights the need for more high-resolution multi-proxy reconstructions with a robust chronological framework to address the challenges posed by spatial and temporal heterogeneity in palaeoclimatic data from the region.

In this study, we reconstructed mid- to late-Holocene ISM variability (~6357 to 298 cal yrs. BP) using an integrated multi-proxy approach supported by AMS radiocarbon dating from the Hulas Khera section (periphery of Karela Lake in the CGP). Hulas Khera section, with its continuous sedimentary succession and favorable depositional setting, provides an ideal opportunity to address the limitations mentioned above. High-resolution sampling, coupled with analysis of sediments using mineral magnetism, sedimentary grain size, and CN analysis, helped in (i) characterizing the nature and source of magnetic minerals and their palaeoenvironmental significance; (ii) interpret depositional environments and sedimentological characteristics reflecting monsoon driven changes; (iii) reconstructing ISM variability over the studied time frame; (iv) examining the role of global forcings in modulating ISM oscillations. The inferred climatic changes during the studied time frame were compared with other regional palaeoclimate records and forcing factors, thereby allowing a broader spatio-temporal perspective of climate dynamics in CGP.

2. Study Area

Hulas Khera (26°41′03.6″N, 81°00′38.71″E) is situated approximately 30 km southeast of Lucknow city (Capital of Uttar Pradesh) and lies in the vicinity of an oxbow lake named 'Karela jheel' (jheel = lake) (Fig. 1). Karela Lake is a meander cutoff lake situated in the Gomti-Sai interfluve, formed from an abandoned channel of the Sai River, which presently flows approximately 10 km south of the lake (Chauhan et al., 2015; Singh, 2005). The presence of the lake made the area suitable for habitation, and its abundance allowed the culture to flourish. Archaeological excavations at the Hulas Khera mound on the southern flank of the Karela Lake have uncovered evidence of human settlement dating to around 1000 BCE (Tewari et al., 1996).

2.1. Geology & Geomorphology

The CGP is part of the broader Indo-Gangetic Plain, a dynamic fluvial basin shaped by complex geological and geomorphological processes. Geologically, the CGP consists predominantly of thick alluvial deposits derived from major river systems. These sediments occupy tectonically formed depressions bounded by the Himalayas in the north and the Bundelkhand Craton to the south, forming the world's largest alluvial expanse over millennia of continuous sedimentation (Singh, 1996, 2005). The geology of the region is also influenced by tectonic activity associated with the uplift of the Himalayas, which has resulted in the formation of a typical foreland basin (Singh, 2005). Geomorphologically, the region is punctuated by a broad network of active and abandoned river channels, interfluves, and undulating surfaces. The area demonstrates a diversity of landforms, including floodplains, naturally leveed riverbanks, abandoned channel belts, meander cutoffs, and aeolian ridges, all of which reflect ongoing interactions among tectonic uplift, sedimentation, and monsoon-driven climatic variability (Singh, 1996). These features formed mainly during the Late Quaternary due to fluctuating climate, base-level changes, and intrabasinal tectonics (Singh, 1996, 2005). Distinct geomorphic features, such as ponds, lakes, and numerous stagnant water bodies, are prevalent, especially in interfluve areas elevated 2 to 10 m above river valleys, such as those of the Gomati and Sai rivers. Many of these lakes are recharged primarily by monsoonal rainfall and local runoff rather than river inflows. These geomorphic features and water bodies are vital for understanding past and present fluvial dynamics, climate variability, and human adaptation in the CGP. They act as key indicators of sedimentary processes, hydrological regimes, and environmental change and support agriculture and water resource management in the region.

2.2. Climate

The climate of the study area is primarily influenced by the ISM and is characterized as a humid subtropical type with dry winters (Cwa according to the Köppen classification) as experienced in the CGP (Chauhan et al., 2018). The southwest monsoon accounts for approximately 80% of the annual rainfall across the CGP, with a distinct precipitation gradient where eastern parts of the Ganga Plains receive higher rainfall than western regions, and northern areas generally receive more precipitation than southern parts. CRU TS 4.07 gridded climate data (Harris et al., 2020) for 1901–2022C.E. was used to create the Walter and Lieth diagram (Walter and Lieth, 1967) for the study area. Analysis of the Walter and Lieth climate diagram in Fig. 1D reveals that the mean annual temperature is 25.5 °C, with June being the hottest

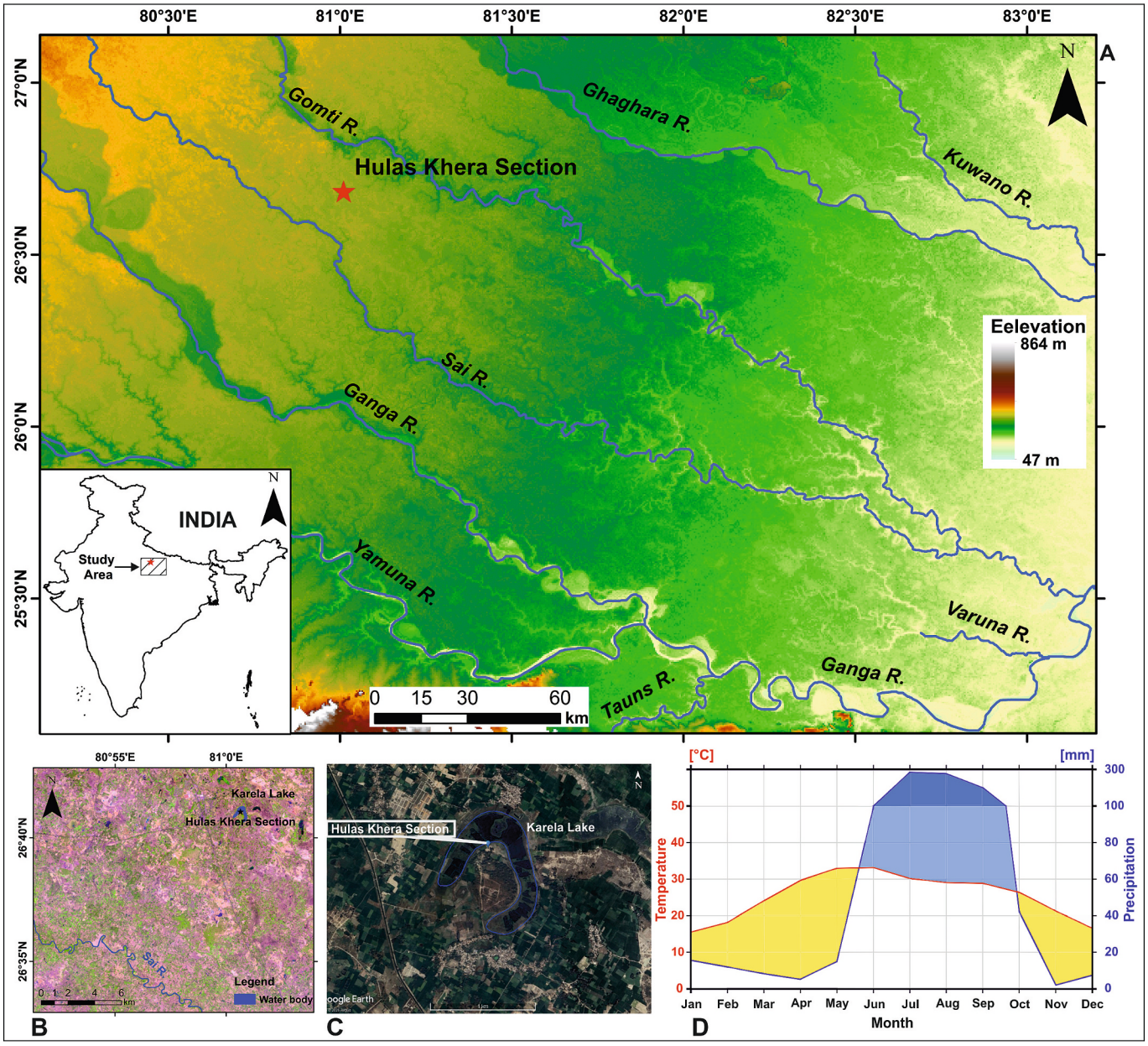

Fig. 1. A. DEM highlighting major river systems and the location of Hulas Khera section. Inset map shows the regional context of the study area with India, B. False-colour satellite imagery of the study area along with Sai River and Karela Lake, C. Google Earth image of the study area showing the extent of Karela Lake and sampling site. D. Walter-Lieth climate diagram (Walter and Lieth, 1967) for the study area based on CRU TS 4.07 gridded climate data (1901–2022C.E.) (Harris et al., 2020). The red line represents the mean monthly temperature (°C), and the blue line shows the mean monthly precipitation (mm). Modified from a diagram generated using ClimateCharts.net (Zepner et al., 2021). (For interpretation of the references to colour in this figure legend, the reader is referred to the web version of this article.)

month (33.2 °C) and January the coolest (15.5 °C). The mean annual precipitation is approximately 969 mm, with July (284.7 mm) being the wettest and November (2.0 mm) the driest month. Consistent with regional patterns, the area receives 88.9% (861.4 mm) of its annual precipitation during the monsoon season from June to September. The strong seasonality of precipitation, with minimal rainfall during winter months, underscores the region's crucial reliance on monsoonal moisture transport for water resources and agricultural activity.

3. Materials and Methods

A ~ 91 cm deep trench was excavated in Hulas Khera (HK) on the periphery of Karela Jheel (26°41′03.6″N, 81°00′38.71″E) to collect sediment samples for the analysis of physical proxies related to sediment characteristics and climatic variations. A total of 70 sediment samples, each approximately 100 g, were retrieved at regular intervals along the trench profile. The selected flank offered an ideal site for sampling due to its compact nature and elevated position, which ensured the preservation of the sedimentary record. These samples form the basis of the present investigation into sediment profile characteristics and palaeoclimatic reconstruction.

3.1. AMS chronology

Three Accelerator Mass Spectrometry (AMS) radiocarbon dates from the HK section were obtained from bulk organic-matter-rich sediment

samples. Samples were dated using the AMS radiocarbon facility at the Inter-University Accelerator Centre (IUAC), New Delhi, India, to establish the chronology. Sediment samples were pre-treated using the Acid–Base–Acid (ABA) protocol to remove contaminants, followed by the preparation of graphite targets with automated graphitization equipment (AGE). Radiocarbon analyses were performed on an accelerator mass spectrometer based on a 500 kV Pelletron accelerator with appropriate primary and secondary standards and process blank (Sharma et al., 2019). The radiocarbon ages were calibrated using the OxCal v4.4.4 (Bronk Ramsey, 2021) and the IntCal20 calibration curve (McKay et al., 2021; Reimer et al., 2020). Since radiocarbon ages alone cannot provide absolutely dated chronologies for palaeoclimatic investigations, a Bayesian age-depth model was employed. The calibration and modelling were performed using the 'Bchron' package in R software (Haslett and Parnell, 2008; McKay et al., 2021; Parnell, 2016; Reimer et al., 2020; R Core Team, 2019).

3.2. Mineral Magnetism

Mineral magnetic parameters were measured following standard procedures (Walden et al., 1999). Raw bulk sediment samples were mechanically disaggregated using an agate mortar and pestle, then homogenized for mineral magnetic measurements. The samples were air-dried and packed into standard 10 cm^3 non-magnetic plastic vials. Mass-specific magnetic susceptibility was measured at two frequencies: low ($\chi_{lf} = 0.976$ kHz) and high ($\chi_{hf} = 15.616$ kHz) using an AGICO MFK2 (Multifunction Kappabridge 2) (Hrouda, 2011). The frequency-dependent susceptibility ($\chi_{fd} = \chi_{lf} - \chi_{hf}$) and the corresponding percentage frequency-dependent susceptibility, $\chi_{fd}\% = 100 \times (\chi_{lf} - \chi_{hf}) / \chi_{lf}$, were calculated to estimate the concentration of fine-grained superparamagnetic (SP) particles (Dearing, 1999; Hrouda, 2011).

Anhysteretic Remanent Magnetization (ARM) was imparted to the samples using an ASC Scientific D-2000AF demagnetizer (with ARM attachment) under a constant DC bias field of 0.05 mT, superimposed on a decaying alternating field with a peak amplitude of 100 mT and a decay rate of 0.001 mT per cycle. ARM susceptibility (χ_{ARM} = ARM/DC bias field) was calculated by normalizing the mass-specific ARM to the DC bias field (0.05 mT = 39.79 A/m) (Liu et al., 2012; Walden et al., 1999).

Isothermal Remanent Magnetization (IRM) was induced in selected samples at field strengths of 20, 100, 200, 300, 500, 800, and 1000 mT, followed by backfield demagnetization at 30 and 300 mT using an ASC Scientific IM-10–30 impulse magnetizer. Magnetic remanence at each IRM acquisition step was measured using an AGICO JR-6 spinner magnetometer. The IRM acquired at 1000 mT was taken as the saturation isothermal remanent magnetization (SIRM).

The S-ratio ($|IRM_{-300mT}|$ / SIRM), soft IRM (SIRM – $|IRM_{-30mT}|$), and hard IRM (SIRM – $|IRM_{-300mT}|$) were calculated to estimate the relative proportions of low-coercivity ferrimagnetic (magnetite, maghemite) and high-coercivity antiferromagnetic (hematite, goethite) minerals (Evans and Heller, 2003; Liu et al., 2012; Thompson and Oldfield, 1986). Inter-parameter ratios χ_{ARM}/SIRM, χ_{ARM}/χ_{lf}, and SIRM/χ_{lf} were calculated to estimate magnetic grain/domain size. A high SIRM/χ_{lf} ratio indicates coarser magnetic grains, whereas elevated χ_{ARM}/SIRM and χ_{ARM}/χ_{lf} values indicate finer grains (Evans and Heller, 2003). Table 1 lists the mineral magnetic parameters studied and their interpretations.

3.3. Grain size Analysis & End-member Modelling Analysis (EMMA)

To characterize the distribution of sand, silt, and clay particles throughout the HK section, a comprehensive grain size analysis was conducted using a laser diffraction particle-size analyzer (Beckman Coulter LS™ 13,320). Systematic removal of carbonate and organic components was achieved through chemical pre-treatment. Approximately 1 g of air-dried, homogenized sediment from each sample was processed following standardized chemical protocols. Carbonate removal was achieved by treating samples with 10% hydrochloric acid (HCl), followed by organic matter removal through treatment with 30% hydrogen peroxide (H_2O_2) (Battarbee et al., 2001; Vaasma, 2008). To prevent grain flocculation during analysis, a 1% solution of sodium

Table 1
Mineral magnetic parameters, instrumentation, and their interpretation (Basavaiah et al., 2021; Dearing et al., 1997; King et al., 1982; Liu et al., 2012; Phartiyal et al., 2024; Snowball and Thompson, 1990; Thompson and Oldfield, 1986).

Mineral Magnetic Parameter & their Units	Mineral Magnetic Parameter & their Units	Interpretation	Climatic Inference
Magnetic Concentration Parameters	Low and High frequency magnetic Susceptibility, χ_{lf} & χ_{hf} ($10^{-8}m^3kg^{-1}$)	Concentration of bulk magnetic minerals present in the sediment sample.	Higher values indicate higher detrital influx.
	Frequency dependent susceptibility χ_{fd} ($10^{-8}m^3kg^{-1}$)	Concentration of Superparamagnetic Grains.	Higher values indicate greater pedogenic magnetite in the catchment.
	Susceptibility of Anhysteretic Remanent Magnetisation χ_{ARM} (10^{-8} m^3 kg^{-1})	Indicates the concentration of ferrimagnetic grains in the stable single-domain (SSD) grain size range	Higher values signify increased pedogenic magnetite influx reflecting enhanced catchment rainfall, whereas lower values indicate reduced precipitation, which is diagnostic of arid phases.
	Saturation Isothermal Remanent Magnetisation SIRM (10^{-5} Am^2kg^{-1})	Approximates the concentration of all remanence-carrying magnetic minerals in a sample.	Higher values reflect increased detrital influx in the catchment, and vice versa.
Magnetic Grain Size Parameters	χ_{ARM}/χlf	Indicates magnetic grain sizes; higher ratios indicate finer grains and vice versa.	Higher ratio values indicate an increased influx of fine SSD and SP grains, whereas lower values reflect a coarser MD grain influx.
	χ_{ARM}/SIRM (10^{-5} mA^{-1})	Higher ratios denote finer magnetic grain size (SSD to SP grains), whereas low values indicate coarser PSD, MD grains.	Higher ratios suggest an increased influx of fine magnetic grains associated with elevated rainfall, whereas very low ratios reflect coarser grain sizes characteristic of anthropogenic sources.
	SIRM/χ_{lf} (10^3Am^{-1})	The Magnetic Grain Size indicator and higher values suggest the presence of authigenic greigite.	Higher ratios represent reducing conditions, typically associated with increased authigenic greigite in oxygen-depleted lacustrine settings.
Magnetic Mineralogical Parameters	Soft IRM (SIRM-$|IRM_{-30mT}|$) ($10^{-5}Am^2kg^{-1}$)	Soft IRM values indicate the presence of low-coercivity minerals, such as magnetite.	Higher values indicate the presence of low-coercivity minerals such as magnetite.
	Hard IRM (SIRM-$|IRM_{-300mT}|$) ($10^{-5}Am^2kg^{-1}$)	Indicative of the concentration of high-coercivity antiferromagnetic minerals, such as hematite and goethite.	Higher HIRM values indicate an increased influx of high-coercivity minerals such as hematite and goethite, reflecting warm, oxidising depositional conditions.
	S-ratio (IRM_{-300mT}/SIRM)	Indicates the relative abundance of low and high-coercivity magnetic mineral concentration in bulk samples.	S-ratio quantifies the relative abundance of ferrimagnetic versus antiferromagnetic minerals. Values close to 1 indicate dominance of low-coercivity minerals, while values close to 0 indicate high-coercivity mineral dominance.

hexametaphosphate $(NaPO_3)_6$ was added as a dispersant (Andreola et al., 2004; Murray, 2002). Before instrumental analysis, samples were ultrasonicated for 1 min at 2400 rpm to ensure complete particle dispersion. Based on the analyses, results were categorized into sand (>63 μm), silt (4–63 μm), and clay (<4 μm) fractions according to the Wentworth grain size classification system (Wentworth, 1922). Statistical analysis and grain-size classification were conducted using GRADISTAT v8 software (Blott and Pye, 2001).

End-member modelling analysis (EMMA) is a multivariate statistical approach to decompose the complex grain size distribution (GSD) data into constituent end-member components. This methodology employs a quantitative approach for palaeoclimatic reconstruction by systematically unmixing polymodal grain size data into genetically distinct subpopulations that reflect sediment sources, transport mechanisms, and depositional regimes (Dietze and Dietze, 2019; Paterson and Heslop, 2015; Prins and Weltje, 1999; van Hateren et al., 2018). To statistically classify grain-size distributions (GSDs) and establish their relationship with lithostratigraphic units, we applied EMMA using the R package EMMAgeo (Dietze and Dietze, 2019; Dietze et al., 2022). Non-parametric end-member modelling or unmixing analysis (EMMA) describes a multidimensional grain-size data set X (m samples × n size classes) as a linear combination of transposed end-member loadings V^T (genetically meaningful subpopulations), end-member scores M (their relative contributions), and an error matrix E, such that-.

$X = M.V^T + E.$

(Aitchison, 1986). EMMAgeo's core EMMA () function implements the MATLAB algorithm of Dietze et al. (2012), using eigenspace analysis with Varimax rotation: the m × n matrix is rescaled to constant row sums, weighted, eigenvectors are extracted and rotated, and end-member scores are calculated via non-negative least squares.

3.4. CN Analysis

Sediment samples were air-dried at 25–30 °C to minimize soil nitrogen loss, then gently crushed and sieved through a 106 μm (150-mesh) sieve to obtain a homogeneous fine fraction. Prior to total organic carbon (TOC) determination, all samples were acid-treated to remove inorganic carbon (carbonates). The decarbonated residues were then rinsed, dried, and prepared for analysis. Total Carbon (TC) and total nitrogen (TN) contents were analyzed on untreated bulk sediment. Carbon and Nitrogen measurements were determined using an Elementar™ Vario MACRO Cube (CHNS-O) analyzer, which employs flash combustion design with an oxidation–reduction system (double furnace) configuration and chromatographic gas separation. Approximately 100–150 mg of sample was weighed into 6 × 12 mm tin boats whose exothermic combustion enhances sample oxidation. Sample boats were weighed on a Sartorius Quintix microbalance (±0.0001 mg sensitivity). The pellets were then loaded into the autosampler carousel and analyzed automatically using the Vario MACRO Cube software. The samples were oxidized in the oxidation furnace (combustion tube) in the presence of oxygen at high temperature (1150 °C). Resulting byproducts of combustion, i.e., CO_2 and oxides of nitrogen gases, were separated via selective adsorption columns. The concentrations of Carbon and Nitrogen are quantified sequentially by a thermal conductivity detector (TCD) using helium as the flushing and carrier gas. Reproducibility was checked using sulfanilamide standards, yielding standard deviations of ±1% for Carbon and ± 0.4% for Nitrogen.

4. Results

4.1. Chronological framework, Lithology, and Age-Depth model

The ^{14}C AMS chronology from the HK section encompasses ~6358–298 cal yrs. BP, thereby providing a continuous record from the mid- to late-Holocene in the CGP. The chronological framework and age–depth model are presented in Table 2 and Fig. 2, respectively. The lithological characteristics of the HK sediment profile (Fig. 2) were initially described through field observations and subsequently validated by sediment textural analysis. The HK section attains a total thickness of 91 cm and is predominantly composed of fine-grained, greyish silty clay. The grain-size distribution indicates that the sediments consist mainly of fine to coarse silt, with occasional intercalations of fine sand at discrete depth intervals. Additionally, calcrete horizons occur at multiple depths, indicating episodes of pedogenic carbonate formation. The profile also contains archaeological inclusions, consisting of potsherds of varying colors and dimensions, burnt pottery fragments, and charcoal remains, which are embedded within the sediment matrix and provide important cultural context.

4.2. Sediment Transport Dynamics: C-M Diagram and End-Member Modelling

The C-M diagram, a logarithmic bivariate plot correlating the coarsest one percentile (C) with the median grain diameter (M) of sedimentary samples (Passega, 1964), provides diagnostic insights into sediment transport and depositional processes. In the modified C–M diagram of the HK profile (Fig. 3A), most samples cluster within Passega's “T” field (light blue; Passega, 1964) and Ludwikowska-Kędzia's corresponding “S” field (dark grey; Ludwikowska-Kędzia, 2000). This clustering indicates deposition within an overbank pool facies, characterized by low-energy, uniform sedimentation, dominated by suspension settling in calm water. The absence of sample points in the R–Q (river-axial/graded suspension), Q–P (siltation and rolling grains), and P—O (active rolling) fields further indicates a lack of high-energy active fluvial channel facies deposition, reinforcing the interpretation of a calm, mostly still water depositional condition.

To complement this, nonparametric EMMA was applied to the bulk grain-size dataset of the HK section, resolving four statistically robust end-members (EM1–EM4) (Fig. 3B, C). EM1 (mean size 8.9 μm) represents a mixed fine assemblage dominated by silt (53.41%), with substantial clay content (23.89%) and sand (22.70%). EM2 (mean size 53 μm) is silt-rich (69.39%) with minimal clay (5.16%) and considerable sand (25.44%). Contrastingly, EM3 (mean size 92 μm) is strongly sand-dominated (75.51%) with lower silt (16.46%) and minimal clay (8.03%). Finally, EM4 (mean size 160 μm) comprises predominantly sand (59.10%), though it retains significant silt (32.92%) and minor clay (7.98%), forming a silty-sand facies associated with fluctuating energy conditions. The grain-size signatures of EM1 and EM2 (8.9–53 μm), representing the fine-to-coarse silt domain, suggest deposition under enhanced surface runoff conditions associated with high seasonal precipitation, likely linked to intensified ISM precipitation. In contrast, the coarser fractions of EM3 and EM4 (92–160 μm), within the fine sand domain, are interpreted as synchronous with episodes of extended dry periods and monsoon minima, when reduced precipitation and runoff favored the transport and deposition of coarser sediments.

Table 2
Details of the radiocarbon ages obtained by accelerator mass spectrometry ^{14}C dating for the HK sediment profile.

Sample ID	Depth (cm)	LAB ID	Radiocarbon Age (years)	Calibrated Age Range (1 Sigma) cal years BP	Median Age (cal years BP)
HK-10	13	IUACD#22C5480	868 ± 34	728–791	764
HK-33	42.9	IUACD#22C5481	2729 ± 33	2780–2849	2818
HK-65	84.5	IUACD#22C5482	5071 ± 43	5751–5898	5815

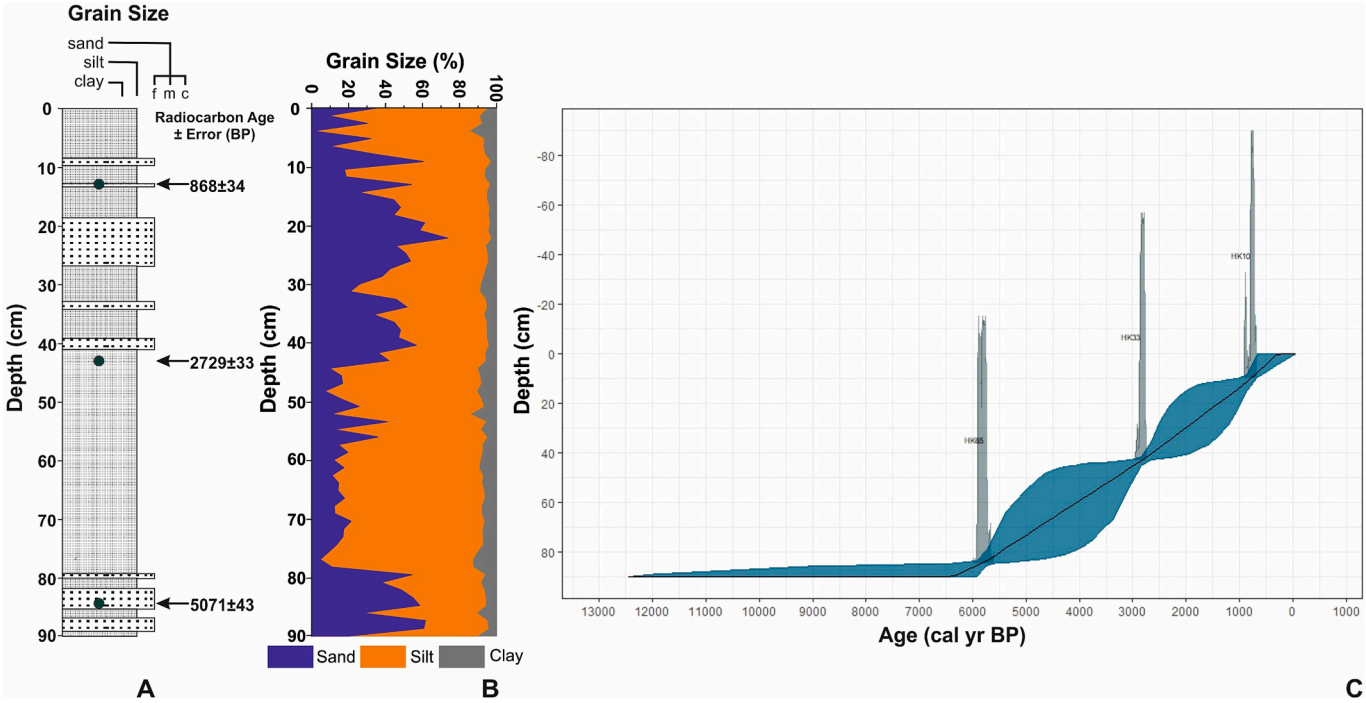

Fig. 2. A. Lithology with AMS ^{14}C ages; B. Variation of sediment grain size with depth; B. Age depth model of HK sediment profile.

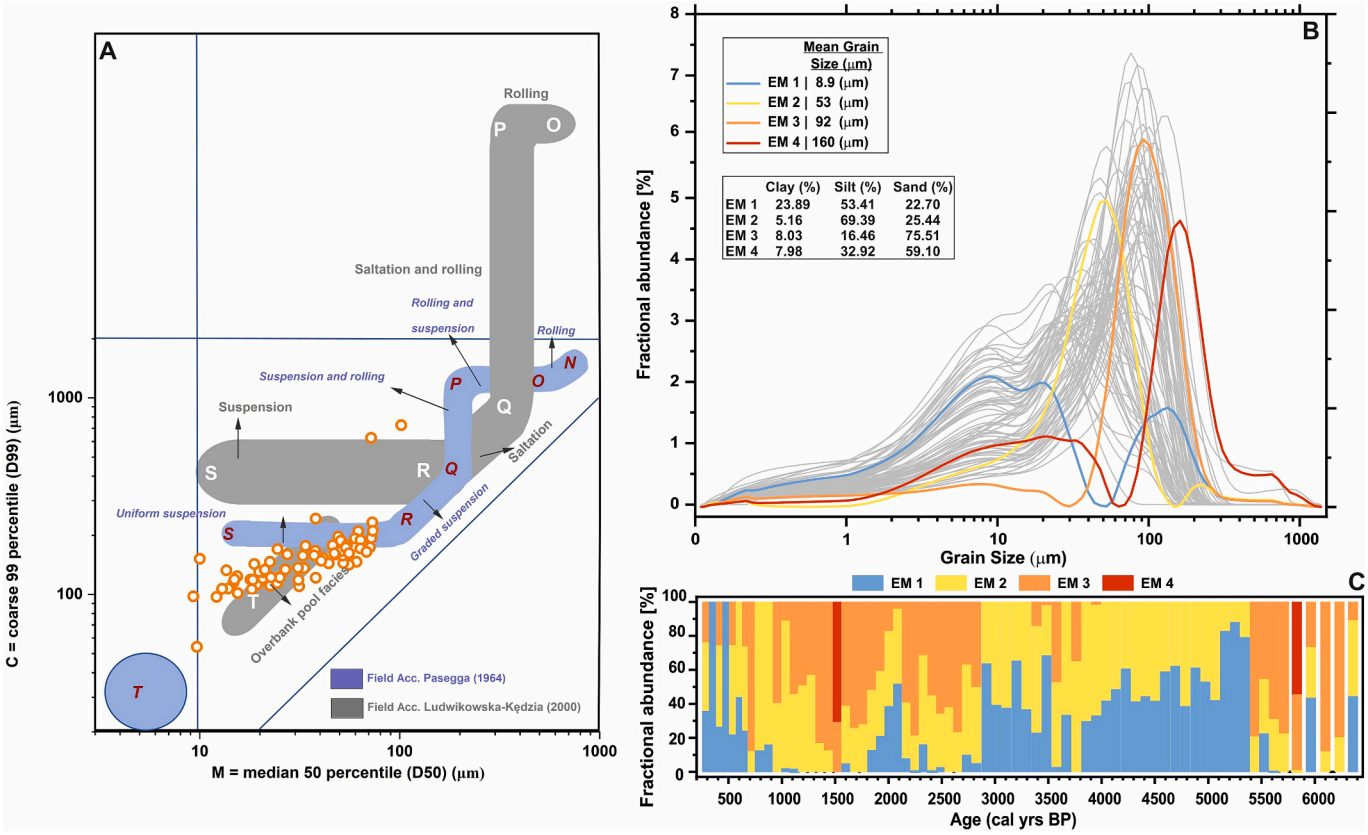

Fig. 3. A. C-M diagram showing the characteristics of the HK sediments. Light blue fields: Passega (1964) and dark grey fields: modified acc. Ludwikowska-Kędzia (2000). Open orange circles show the HK samples; B. Grain Size distribution of EM 1–4 (Light grey curves denote the bulk grain size distribution of the sediment samples); C. EM abundance (temporal variability of end-member contributions across sediment sequence). (For interpretation of the references to colour in this figure legend, the reader is referred to the web version of this article.)

4.3. Palaeoclimatic reconstruction

Constrained Incremental Sums of Squares (CONISS) cluster analysis was performed on the combined textural, mineral magnetic, and CN proxy datasets using TILIA 1.7 (Grimm, 1987, 1990). The analysis delineated seven distinct significant stratigraphic zones (HK-1 to HK-7), each reflecting distinct environmental conditions (Fig. 4). These zones represent shifts in depositional regimes, ISM variability, and organic productivity, thereby providing a robust framework for reconstructing the Holocene climatic evolution of the HK section.

4.3.1. Climate Zone HK 1 (91.0–78 cms; 6358–5251 cal yrs. BP)

This zone, spanning ~1100 years, is characterized by a high influx of sand (4.6–61.6%) and silt (33.2–82.4%), with comparatively lower clay content (4.6–12.97%). The mean grain size (9.3–57.6 μm) exhibits substantial variability, reflecting fluctuating depositional energy conditions. EMMA indicates variable contributions from silt-sized populations EM1 (8.9 μm; mean 25.5%) and EM2 (53 μm; mean 22.4%), interpreted as signals of enhanced surface runoff during ISM phases. In contrast, the presence of EM3 (92 μm; mean 47.2%) reflects increased fine-sand input under comparatively drier, low-energy conditions.

Magnetic concentration parameters show relatively low χ_{lf} (23.4–33.5 × 10^{-8} m^3kg^{-1}) and χ_{ARM} (112.4–142.3 × 10^{-8} m^3kg^{-1}) values, while SIRM (133.8–232.0 × 10^{-5} Am^2kg^{-1}) exhibits moderate concentrations. Magnetic mineralogy parameters, including the S-ratio (0.87–0.98), Soft IRM (91.42–160.7 × 10^{-5} Am^2kg^{-1}), and HIRM (4.3–22.1 × 10^{-5} Am^2kg^{-1}), indicate a mixed magnetic mineralogy. Magnetic grain-size parameters, such as $\chi_{ARM}/SIRM$ (4.3–22.1 × 10^{-5} mA^{-1}), χ_{ARM}/χ_{lf} (4–5.35), are low relative to $SIRM/\chi_{lf}$ (5.6–7.6 × 10^3 Am^{-1}), collectively suggesting a predominance of coarser magnetic grains associated with arid phases.

The elemental data show that TC concentration ranges between 1.63 and 1.8%, while TN is consistently low (0.01 to 0.02%). The resulting atomic C/N ratios or TOC/TN (18.5–42.0) are notably high, pointing to a dominance of terrestrial organic matter inputs. The geochemical signatures align with the grain-size evidence, suggesting that terrestrial OM was transported to the depositional setting under variable-energy conditions, controlled by fluctuations in watershed runoff.

4.3.2. Climate Zone HK 2 (78–45.5 cms; 5251–2920 cal yrs. BP)

This ~2300-year interval is dominated by silt fractions ranging between 53.2 and 82.1% in contrast to lower sand 7.2–40.9% and clay 5.4–14.5% fractions, with mean grain size varying between 10.1 and 33.8 μm, indicating a predominantly fine-grained input under low energy hydrodynamic conditions. EMMA reveals alternating silt populations EM1 (mean 44.7%), EM2 (mean 51.3%), and minor EM3 (mean 4%), reflecting shifts between primary fine silt and occasional coarser sediment pulses. Magnetic concentration parameters χ_{lf} (23.5–42.6 × 10^{-8} m^3kg^{-1}), χ_{ARM} (122.6–175.8 × 10^{-8} m^3kg^{-1}), and SIRM (136.1–362.8 × 10^{-5} Am^2kg^{-1}), show a modest increasing trend relative to HK1, with enhanced variability, particularly in SIRM which peaks sporadically and χ_{fd}% (3.3–13.5%) averaging 8.2% represents significant superparamagnetic contribution. S-ratio (0.63–0.99), Soft IRM (92.8–320.9 × 10^{-5} Am^2kg^{-1}), and HIRM (3.1–73.2 × 10^{-5} Am^2kg^{-1}) remain high but with broader fluctuations, denoting a continued ferrimagnetic mineral assemblage with intermittent high coercive mineral presence. $\chi_{ARM}/SIRM$ (45.1–90.9× 10^{-5} mA^{-1}), χ_{ARM}/χ_{lf} (3.89–5.40) remain high, and $SIRM/\chi_{lf}$ (5–10.1 × 10^3 Am^{-1}) is low, representing the presence of finer magnetic grain distribution. The TC and TOC concentrations in this zone vary between 1.74 and 2.14% and 0.40–0.62%, respectively. The TN concentration in this zone varies between 0.01 and 0.04%. In contrast, TOC/TN in the sedimentary organic matter ranged from 10.3 to 46. Like the climate zone HK 1, in this zone, high TOC/TN ratios also suggest terrestrial organic input; however, with relatively less energy than in HK 1.

While two short periods of sustained dryness are punctuated as Subzones HKZ 2a between (4411–4228 cal yrs. BP) and HKZ 2b (3669–3483 cal yrs. BP). HKZ 2a shows a dominant coarser magnetic grain size and lower χ_{fd}%, followed by TOC/TN ratios. In contrast, HKZ 2b is characterized by a lower S-ratio and a higher HIRM, indicative of a

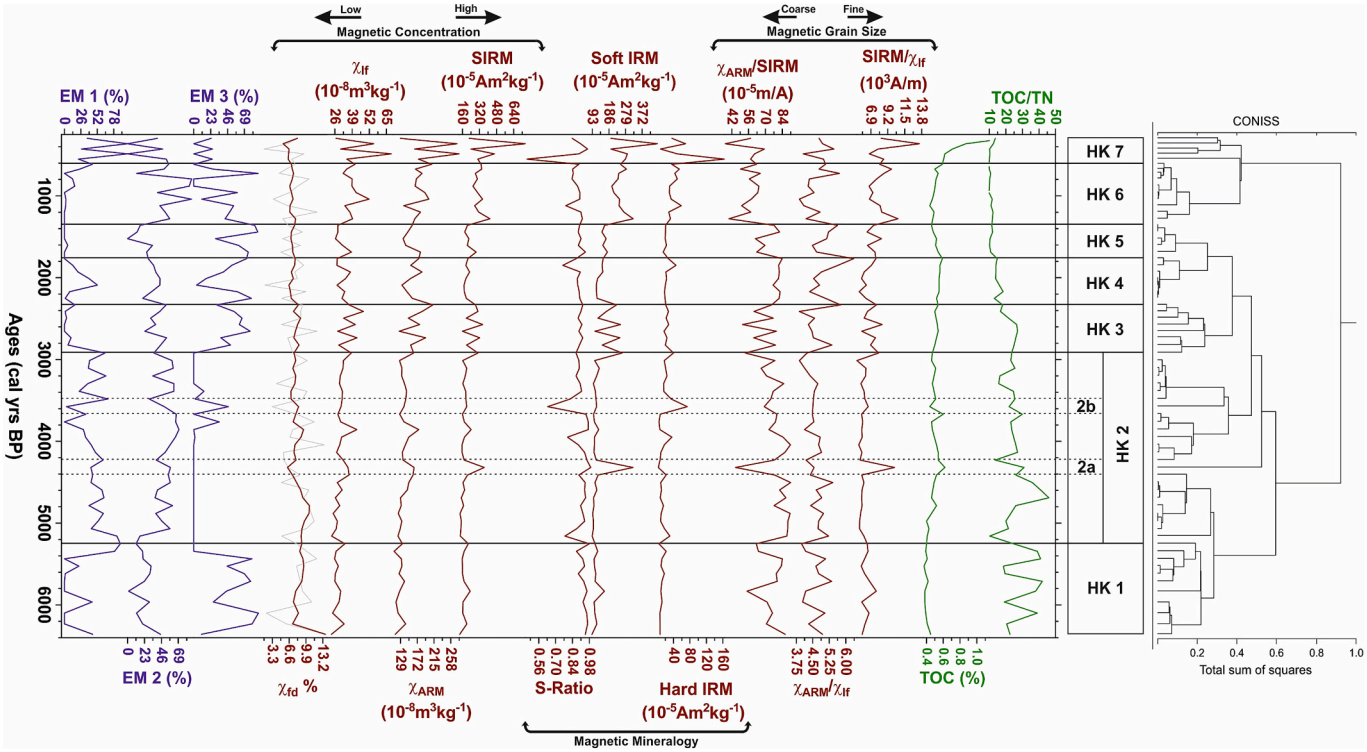

Fig. 4. Variations in the Physical (EM1, EM2, EM3, EM4, χ_{lf}, χ_{ARM}, S-ratio, SIRM, Soft IRM, Hard IRM, $SIRM/\chi_{lf}$, χ_{ARM}/χ_{lf}, $\chi_{ARM}/SIRM$) and TOC%, TOC/TN ratio plotted for the HK sediment profile.

high-coercivity magnetic mineralogy, along with a coarser magnetic grain size, as evidenced by higher EM3 and lower TOC.

4.3.3. Climate Zone HK 3 (45.5–36.4 cms; 2920–2332 cal yrs. BP)

This zone represents a period of ~600 years, depicting variable depositional conditions changing sand, silt, and clay input, fluctuating end-member contributions, variable magnetic properties, and sustained terrestrial organic influx. Sand content varying between 33.5% to 56.6%, silt from 38.9% to 59.6%, and clay from 4.5% to 6.9%, with mean grain size oscillating between 27.9 μm and 48.7 μm, suggesting periodic changes between stronger and weaker hydrodynamic conditions. EM1 (mean 5.2%), EM2 (mean 41%), and EM3 (mean 53.8%) reflecting alternating fine-silt and coarse-silt/fine-sand inputs. Low-field susceptibility χ_{lf} (28.2–47.5 $\times 10^{-8}$ m^3kg^{-1}), χ_{ARM} (125.9–211.9 $\times 10^{-8}$ m^3kg^{-1}), and SIRM (159.3–348.6 $\times 10^{-5}$ Am^2kg^{-1}) are higher concentrations but with fluctuating trend, and $\chi_{fd}\% = 5.1–12.1\%$ indicating moderate presence of SP grains. S-ratio (0.89–0.93), Soft IRM (108.3–251.0 $\times 10^{-5}$ Am^2kg^{-1}), and HIRM (16.9–28.4 $\times 10^{-5}$ Am^2kg^{-1}) suggest mixed magnetic mineralogy. Magnetic grain-size indicators χ_{ARM}/SIRM (51–79 $\times 10^{-5}$ mA^{-1}), χ_{ARM}/χ_{lf} (3.9–5.76), and SIRM/χ_{lf} (5.7–8.4 $\times 10^3$ Am^{-1}) point to relatively coarser magnetic grains during peaks in coarse sediment deposition. The TC concentration in this zone varies between 1.99 and 2.28%. The TN concentration in this zone varies between 0.02 and 0.03%. While the atomic C/N (or TOC/TN) in the sedimentary organic matter ranges from 15.7 to 27, a relatively higher TOC/TN ratio may suggest inputs from terrestrial organic sources. The results from this zone are like those of Zone HK 2, with both higher and lower elemental ratios, indicating a shifting trend in energy.

4.3.4. Climate Zone HK 4 (36.4–27.3 cms; 2332–1767 cal yrs. BP)

This period, comprising ~550 years of climatic history, records moderate depositional energy with mixed sediment textures. Sand content ranges from 20.8 to 53.5%, silt from 41.8 to 70.1%, and clay from 4.7 to 9.1%, with a mean grain size of 19.1–47.1 μm. EM1 (mean 19.2%), EM2 (mean 34.8%), and EM3 (mean 46%), indicating alternation between fine silt and coarser fractions. χ_{lf} (27.8–37.7 $\times 10^{-8}$ m^3kg^{-1}), χ_{ARM} (132.5–184.3 $\times 10^{-8}$ m^3kg^{-1}), and SIRM (173.5–226.1 $\times 10^{-5}$ Am^2kg^{-1}) reflect moderate magnetic concentration. $\chi_{fd}\%$ (1.8–9.5%) (mean 7.2%) represents a lesser concentration of SP grains. Magnetic mineralogical parameters point toward a ferrimagnetic-dominated assemblage, with moderate to high S-ratio ranging between 0.76 and 0.91, soft IRM (115.6–153.7 $\times 10^{-5}$ Am^2kg^{-1}), and low HIRM (18.4–46.0 $\times 10^{-5}$ Am^2kg^{-1}). χ_{ARM}/SIRM (76.4–83.9 $\times 10^{-5}$ mA^{-1}), SIRM/χ_{lf} (5.3–7.6 $\times 10^3$ Am^{-1}), and χ_{ARM}/χ_{lf} = 4.4–6.4 point toward finer magnetic grain distributions. The TC and TOC concentrations in this zone vary between 1.59 and 2.09% and 0.52 and 0.59%, respectively. The TN concentration in this zone varies between 0.03 and 0.05%. While the atomic C/N (or TOC/TN) ranged from 13.0 to 18.3, the TOC/TN ratios are relatively lower compared to those in the previous zones (HK 1, HK 2, and HK 3), which may suggest fluctuations in terrestrial organic input. The zone suggests variable climatic conditions, with clear episodes of increased monsoon intensity and terrestrial erosion.

4.3.5. Climate Zone HK 5 (27.3–20.8 cms; 1767–1361 cal yrs. BP)

This zone, spanning ~400 years, is characterized by moderately high sand content (mean 58.0%), lower silt (mean 37.5%), and minimal clay (mean 4.6%), along with variable mean grain size ranging from 35.9 to 86.6 μm, reflecting predominantly coarser sediment input. Sediment EMMA shows low contributions of EM1 (mean 1%) and EM2 (mean 18%), with dominance of the coarser fraction EM3 (mean 66.9%), consistent with a sand-rich sediment supply. χ_{lf} ranging from 26.4 to 38.5 $\times 10^{-8}$ m^3kg^{-1}, χ_{ARM} between 135.6 and 180.1 $\times 10^{-8}$ m^3kg^{-1}, and SIRM spanning 180.3 to 286.8 $\times 10^{-5}$ Am^2kg^{-1}. S-ratio is consistently high (0.89–0.95) along with Soft IRM (147.0–177.4 $\times 10^{-5}$ Am^2kg^{-1}), which exceeds hard IRM concentrations (14.9–22.8 $\times 10^{-5}$ Am^2kg^{-1}), pointing toward a mixed magnetic mineral assemblage. χ_{ARM}/SIRM between 61.6 and 81.8$\times 10^{-5}$ mA^{-1}, SIRM/χ_{lf} ratio range between 6.4 and 8.3 $\times 10^3$ Am^{-1}, and χ_{ARM}/χ_{lf} between 4.5 and 5.6, suggesting dominance of relatively coarser magnetic grains. TC content between 1.4 and 1.8%, TOC ranging between 0.46 and 0.54%, and TOC/TN ratio ranging from 10.2 to 12, indicating sustained terrestrial organic matter input under moderate depositional energy.

4.3.6. Climate Zone HK 6 (20.8–7.8 cms; 1361–613.5 cal yrs. BP)

This zone spanning ~750 years is characterized by higher silt and moderate sand, with low clay, with sand percentages ranging from 9.7% to 60.5%, silt from 36.1% to 83.1%, and clay from 3.4% to 7.2%. The mean grain size ranges from 16.2 μm to 61.6 μm, suggesting varying depositional energy. EM1 is low (mean 10.2%), while EM2 (mean 56.9%) is more prominent. There are also occasional peaks in EM3 (mean 32.9%), suggesting dominance of finer silt, with few episodes of coarser, sand-sized sediment deposition. Magnetic concentration parameters indicate moderate to high concentrations of magnetic minerals as χ_{lf} values range from 32.3 to 51.8 $\times 10^{-8}$ m^3kg^{-1} (mean 39.1 $\times 10^{-8}$ m^3kg^{-1}), χ_{ARM} from 137.5 to 209.0 $\times 10^{-8}$ m^3kg^{-1} (mean 177.3 $\times 10^{-8}$ m^3kg^{-1}), and SIRM from 258.3 to 417.0 $\times 10^{-5}$ A m^2kg^{-1} (mean 316.2 $\times 10^{-5}$ A m^2kg^{-1}). These results suggest an increased input of magnetic minerals during this period. S-ratio varies from 0.78 to 0.92, indicating a ferrimagnetic mineral dominance. Soft IRM values range between 201.9 and 321.8 $\times 10^{-5}$ A m^2kg^{-1} and HIRM between 28.2 and 58.9 $\times 10^{-5}$ A m^2kg^{-1}, pointing to mixed magnetic mineralogy with mainly softer magnetic mineralogy. χ_{ARM}/SIRM (39.7–65.7 $\times 10^{-5}$ mA^{-1}), SIRM/χ_{lf} (6.6–10.6 $\times 10^3$ Am^{-1}), and χ_{ARM}/χ_{lf} (3.9–5.7) reflect a mixture of coarse to moderate magnetic grain sizes, consistent with episodic changes in sediment supply and hydrodynamic conditions. TC ranging from 0.8% to 1.5%, TOC from 0.4% to 0.6%, and TOC/TN atomic ratios between 9.8 and 12.2, indicating persistent terrestrial organic matter influx under moderately varying depositional conditions.

4.3.7. Climate Zone HK 7 (7.8–0 cms;613.5–298 cal yrs. BP)

This short period, covering ~300 years, is characterized by a fluctuating depositional regime. Sand percentage ranges from 0.62% to 35.2%, Silt from 59.6% to 84.5%, and Clay from 5.2% to 14.8%. Mean grain size varies between 8.57 and 32.31 μm, indicating mainly fine sediments with instances of increased coarser inputs. EM1 (mean 57%), EM2 (mean 28.2%), and EM3 (mean 14.9%), showing changes between very fine silt dominance and episodes of coarser sediment input. χ_{lf} ranges from 26.9 to 68.6 $\times 10^{-8}$ m^3kg^{-1}, χ_{ARM} between 128.7 and 279.2 $\times 10^{-8}$ m^3kg^{-1}, and SIRM ranges from 223.3 to 747.9 $\times 10^{-5}$ Am^2kg^{-1}. The S-ratio varies between 0.46 and 0.97, indicating mixed mineralogy. Soft IRM values vary widely between 197.5 and 456.6 $\times 10^{-5}$ Am^2kg^{-1} (mean 283.8 $\times 10^{-5}$ Am^2kg^{-1}), surpassing hard IRM values ranging from 8.1 to 163.3 $\times 10^{-5}$ Am^2kg^{-1} (mean 65.2 $\times 10^{-5}$ Am^2kg^{-1}), consistent with a mixture of soft and hard magnetic minerals. χ_{ARM}/SIRM range from 36.6 to 69.2 $\times 10^{-5}$ mA^{-1}, lower χ_{ARM}/χ_{lf} values vary between 4.08 and 5.5, and high SIRM/χ_{lf} spans 6.7% to 13.5$\times 10^3$ Am^{-1}, indicative of variable grain size distributions with dominance of coarser magnetic grains. TC from 0.85 to 1.44, TOC from 0.6% to 1.4%, and TOC/TN atomic ratios ranging from 10.1 to 13.6, pointing to a relatively stable but variable terrestrial organic matter input.

5. Discussion

5.1. Nature and source of magnetic Minerals in the HK sediments

Magnetic minerals found in lacustrine sediments are mainly derived from detrital input from the catchment. However, before employing the magnetic properties as representative of changes in catchment erosion, others sources of variation in the magnetic properties of sediments should be considered such as detrital input (Liu et al., 2012), dissolution

of magnetic minerals (Anderson and Rippey, 1988), contributions from bacterial magnetite (Kim et al., 2005; Snowball, 1994), anthropogenic magnetite (Gautam et al., 2004), and authigenic greigite formation (Roberts, 1995; Snowball, 1991). Understanding the palaeoenvironmental implications of magnetic proxies, therefore, requires careful consideration of the sources of magnetic minerals and the processes governing their formation. Variations in rock magnetic parameters down-core in the HK Section are illustrated in Fig. 4. In the lacustrine systems, bacterial activity can likely be the cause of magnetic minerals, notably production of magnetosomes by magnetotactic bacteria (Oldfield et al., 2010; Vali et al., 1987) and the synthesis of SSD magnetite grains (diameter ranging from 0.02 to 0.1 μm) (Oldfield et al., 2010). Oldfield (2007) proposed a biplot of χ_{ARM}/χ_{lf} vs. χ_{ARM}/χ_{fd} to distinguish between fine-grained magnetic minerals of detrital and bacterial origins. Fig. 5 shows the biplot with values of χ_{ARM}/χ_{lf} (3.89–6.35) and χ_{ARM}/χ_{fd} (35.35–330.73), indicating that these samples

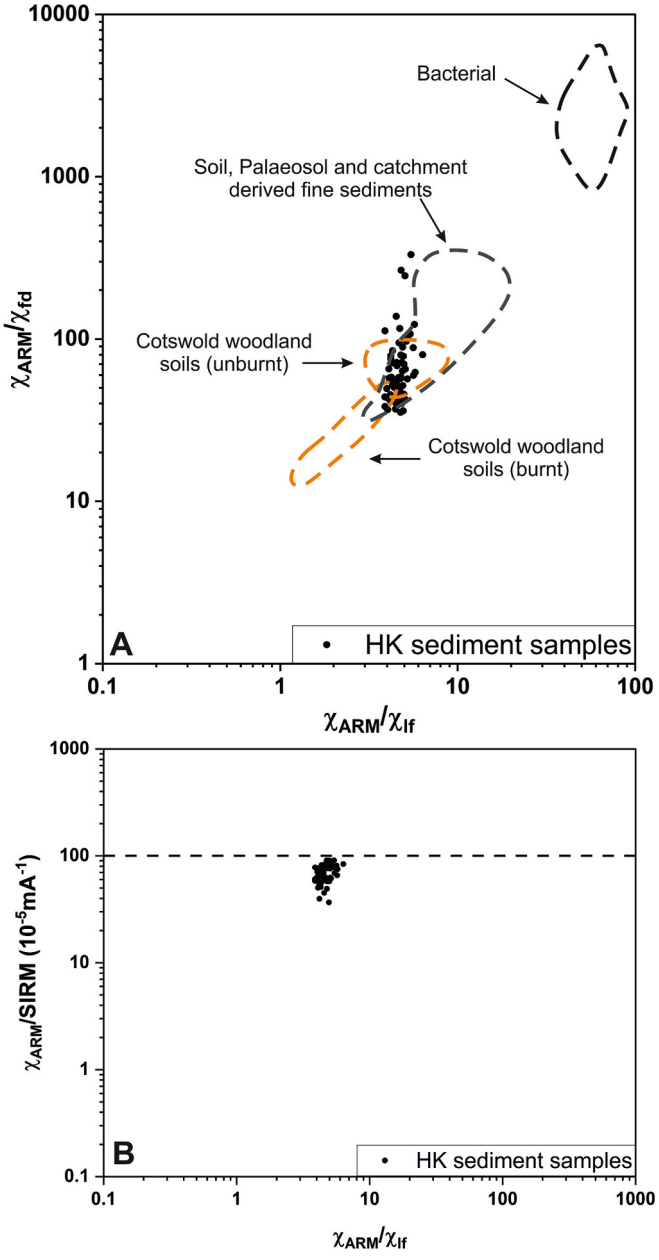

Fig. 5. Bi-plot of A. χ_{ARM}/χ_{lf} vs. χ_{ARM}/χ_{fd} (Oldfield, 2007; Oldfield and Crowther, 2007); B. χ_{ARM}/SIRM vs. χ_{ARM}/χ_{lf} (logarithmic scale) for HK sediment samples.

fall well below the bacterial magnetite range as they are considerably lower than threshold values for bacterial magnetite, i.e., $\chi_{ARM}/\chi_{lf} > 40$, $\chi_{ARM}/\chi_{fd} > 1000$ (Dearing, 1999; Oldfield, 2007). χ_{ARM}/SIRM is also used to decipher the presence of bacterial magnetite if χ_{ARM}/SIRM $>200 \times 10^{-5}$ mA^{-1} (Oldfield et al., 2010), whereas HK sediments yield lower values in the range of 36.63–90.89 $\times 10^{-5}$ mA^{-1} (Fig. 5). Hence, there is no evidence for a significant contribution from bacterial magnetite in the HK sediments. However, magnetic properties related to allochthonous inputs and biogenic/authigenic formation can be significantly altered by reductive diagenesis (Anderson and Rippey, 1988; Oldfield et al., 2010). Hence, the SIRM/χ_{lf} ratio has been used to detect the presence of Greigite (Fe_3S_4), which is one of the potential authigenic contributors to the magnetic mineral assemblages in lake sediments (Roberts, 1995), with $>40 \times 10^3$ Am^{-1} indicating its presence (Dearing, 1999; Oldfield et al., 2010; Snowball, 1991). The value of SIRM/χ_{lf} ranges from 5 to 13.5 $\times 10^3$ Am^{-1} for HK sediment samples (Fig. 4), which is lower than that attributed to its presence. This rules out the presence of greigite, which is ferrimagnetic iron sulphide that forms under anoxic conditions, as a component of the HK sediments' magnetic signature. For a reliable interpretation of a climate or environmental proxy, the potential dissolution of magnetic minerals must also be considered, as fine-grained iron oxides are susceptible to dissolution caused by organic matter oxidation, leading to coarsening of the magnetic grain-size distribution (Anderson and Rippey, 1988). This process results in decreased magnetic concentrations and the removal of finer magnetic grains, reflected in decreasing trends in χ_{ARM}/SIRM and χ_{ARM}/χ_{lf} ratios. Anthropogenic magnetic minerals exhibit distinct magnetic properties compared to magnetic minerals derived from natural sources (Oldfield et al., 1985), particularly in terms of coarser magnetic grain sizes (MD and PSD). The majority of HK sediment samples cluster in the coarse SSD range, with a few in the finer SSD range (Fig. 6), reflecting a lack of coarse-grained magnetic particles. This absence of MD/PSD signatures characteristic of anthropogenic magnetite (Gautam et al., 2004; Maher and Thompson, 1992; Warrier et al., 2014) demonstrates that HK sediments lack detectable anthropogenic contributions to their magnetic signal (Fig. 6). The semi-quantitative analysis of magnetic granulometry can be assessed using χ_{ARM}/SIRM versus χ_{fd}% bi-plots (Dearing et al., 1997). The high χ_{fd}% values in HK sediments (1.65%–13.68%, mean 7.84%) indicate the presence of superparamagnetic (SP) grains originating from pedogenic processes in catchment soils. Numerous studies have shown that tropical soils produce significant amounts of pedogenic magnetite in the SP grain size range (Sandeep et al., 2012). Elevated χ_{fd}% values also suggest enhanced chemical weathering and soil formation during warmer periods. These conditions promote the development of fine-grained magnetic minerals (in the SP and SSD grain size range) through soil-atmosphere interactions.

Variations in detrital influx reflect shifts in catchment erosion driven by changing rainfall patterns, suggesting that precipitation is the primary driver of magnetic property changes in the HK sediments. The analysis represents no detectable contribution from bacterial magnetite, greigite, or anthropogenic processes on the HK magnetic record; hence, the magnetic signal is catchment-derived. All the magnetic parameter signatures indicate that the HK sediments predominantly originated from erosional inputs, supporting a detrital origin for the magnetic signal.

5.2. Depositional Environment and Sedimentological Characteristics of HK sediments

The sedimentological characteristics of the HK sediment record point toward a dominant overbank-pool facies indicated by the C-M diagram (Fig. 3A). The Karela lake was formed from a meander cut-off of the Sai River at around 14,000 cal yrs. BP (Singh, 2005) evidenced by the ox-bow shape of the lake and presence of coarse sand at the base of the exposed section, suggesting the existence of an active channel depicting sediment accumulation under a fluvial environment of the Sai River

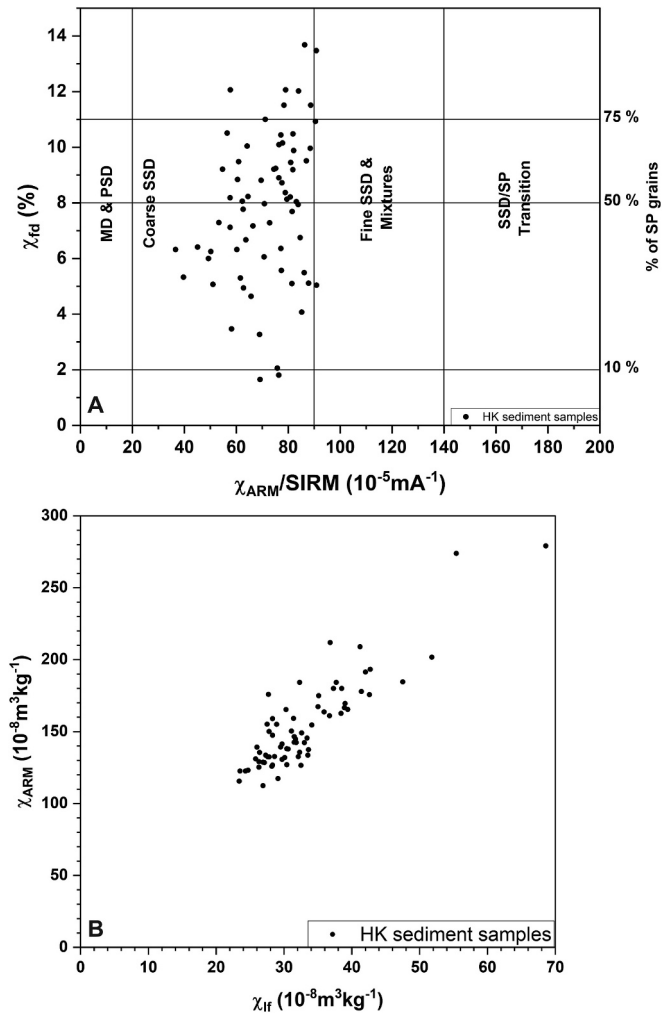

Fig. 6. Bi-plot of A. χ_{ARM}/SIRM vs. χ_{fd} % (Dearing et al., 1997); B. χ_{lf} vs. χ_{ARM} (also known as the King's plot; King et al., 1982), indicating the magnetic grain size for HK sediments.

(Chauhan et al., 2015; Singh, 2005). Grain-size end-member modelling and C-M diagram interpretation collectively indicate that the dominant sediment facies represent suspension fallout in a still-water lacustrine setting, consistent with overbank-pool deposition patterns. The Passega C-M field occupied by most sediment samples displays characteristics of fine-grained suspension and graded suspension with consistently low C-values, representing stagnant-water environments typical of floodplain depressions receiving episodic recharge through sheet flow rather than active channel processes (Passega, 1964). This interpretation gains further support from regional palaeohydrological reconstructions across the CGP, which demonstrate that numerous oxbow lakes experienced complete river disconnection during the mid-Holocene (Chauhan et al., 2015; Saxena et al., 2015; Singh, 1996; Srivastava et al., 2003b).

The key features of sedimentary reconstruction in the HK section are the recurrent deposition of relatively coarse end-member populations (EM3 and EM4), interspersed with finer sediments (EM1 and EM2), reflecting a climatically controlled phenomenon. The small size of Karela Lake makes it exceptionally sensitive to seasonal and multiannual water-level fluctuations; therefore, the HK sediment record shows coarse sediment deposition during dry periods. Palaeoclimatic reconstructions from multiple lacustrine archives demonstrate that the coarse sediment depositional episodes correspond temporally with periods of reduced precipitation and increased dryness, resulting in lake contraction, while finer materials are representative of high lake stand and wetter climatic conditions (Bird et al., 2014; Rawat et al., 2021; Trivedi et al., 2024), supporting their interpretation as drought-stage indicators rather than high-energy fluvial incursions. When extended drought periods are frequent, the lake water level drops, allowing coarse particles to be transported far inwards into the lake. This occurs because gravity separation, driven by the density difference between dense sediment-laden runoff and less dense lake water during rainfall, shifts inwards from the lake margin when water levels are low. Trivedi et al. (2024) also suggested that increased lake hydrology during strong monsoonal conditions led to the deposition of finer sediment EMs, as increased water levels likely limited the inward transport of coarser sediments, enabling finer particles to remain suspended and disperse uniformly throughout the water column.

5.3. Palaeoclimatic reconstruction for the last ~6350 years and regional climatic correlation in the Central Ganga Plain and the role of Global forcing

Palaeoclimatic reconstruction from the HK section (Fig. 4) reveals mid- to late Holocene climatic variations in the CGP. While ISM-driven Holocene climatic variability over the Gangetic Plains has recently been synthesized through regional lake sedimentary records (Misra et al., 2020; Phartiyal et al., 2024; Quamar et al., 2024), previous studies have predominantly relied on biotic proxies (pollen, phytolith, diatoms) (Fig. 7). The present multi-proxy approach combines sediment texture analysis to characterize depositional environments; mineral magnetic parameters to assess sediment flux and lithologic variations; and TOC concentration, along with the TOC/TN ratio, to evaluate palaeoproductivity and terrestrial organic matter input. This integrated approach provides a sedimentological and geochemical perspective that captures direct monsoon-driven catchment responses, complementing existing archives and advancing understanding of ISM-driven Holocene variability in CGP.

5.3.1. HK-1 (6358–5251 cal yrs. BP): Weak Monsoon, Arid climate, and Reduced Lake Productivity

Between 6358 and 5251 cal yrs. BP, mineral magnetic concentration remained generally low with moderate variability, while coarser magnetic grain sizes and negligible SP contributions indicate deposition under drier conditions. Toward the end of this phase, however, a gradual tendency toward slightly finer grains marks the onset of a transition in the depositional environment. End-member modelling confirms the dominance of coarse fractions (EM3, with episodic EM4), suggesting enhanced physical erosion at the exposed lake margins under reduced runoff (Dietze et al., 2012). Organic geochemical proxies reinforce this interpretation. Low TOC levels and high, stable C/N ratios further support limited aquatic productivity and steady terrestrial organic matter input, collectively indicating low lake levels during prolonged ISM weakening, a pattern extensively documented across the middle to late Holocene (Gupta et al., 2003; Overpeck et al., 1996; Phartiyal et al., 2024; Sirocko et al., 1991).

Regionally, this aligns with CGP aridity episodes at Kanwar Wetland linked to ISM weakening and North Atlantic cooling episodes (Phartiyal et al., 2024), channel abandonment and ponding due to reduced rainfall/glacial melt (8–6 ka BP; Srivastava et al., 2003b), mid-Holocene water table decline (Agarwal et al., 1992), and drier pollen assemblages (~8700–4800 cal yrs. BP; Chauhan et al., 2015). Beyond the Ganga Plain, $\delta^{18}O$ enrichment at Tso Moriri, Kotla Dahar, and Lonar Lake confirms progressive ISM decline after ~6000 cal yrs. BP (Misra et al., 2019), alongside strengthened westerlies in the Trans-Himalaya (Nag et al., 2023).

5.3.2. HK-2 (5251–2920 cal yrs. BP): Predominantly Low-Energy Deposition with Episodic Dry Phases

Between 5251 and 2920 cal yrs. BP, fine-grained sedimentation dominated under low-energy hydrodynamic conditions, interspersed with two distinct dry episodes (4411–4228 and 3669–3483 cal yrs. BP).

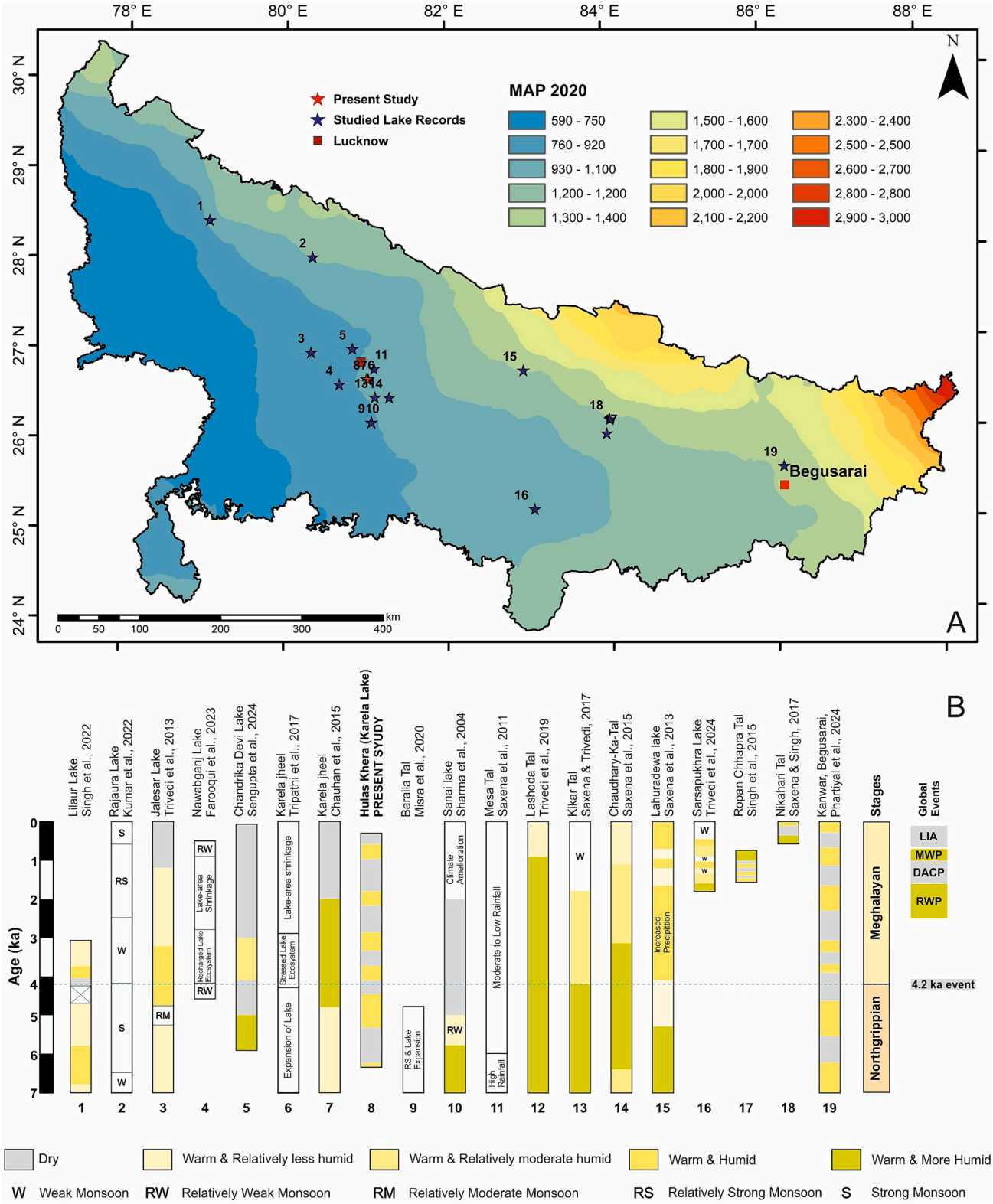

Fig. 7. A. Precipitation gradient across the Ganga Plain plotted using the gridded CRU TS dataset version 4.07 (Harris et al., 2020) with locations of previously studied lake records and the present study; B. Comparison of the HK Dataset with the other studied records from the Ganga Plain - 1. Lilaur Lake (Singh et al., 2022), 2. Rajaura Lake (Kumar et al., 2022), 3. Jalesar Lake (Trivedi et al., 2013), 4. Nawabganj Lake (Farooqui et al., 2023), 5. Chandrika Devi Lake (Sengupta et al., 2024), 6&7. Karela Jheel (Tripathi et al., 2017; Chauhan et al., 2015), 8. Hulas Khera (Present Study), 9. Baraila Tal (Misra et al., 2020), 10. Sanai Tal (Sharma et al., 2004), 11. Mesa Tal (Saxena et al., 2011), 12. Lashoda Tal (Trivedi et al., 2019), 13. Kikar Tal (Saxena and Trivedi, 2017), 14. Chaudhary-ka-Tal (Saxena et al., 2015), 15. Lahuradewa Lake (Saxena et al., 2013), 16. Sarsapukhra Lake (Trivedi et al., 2024), 17. Ropan Chhapra Tal (Singh et al., 2015), 18. Nikahari Tal (Saxena and Singh, 2017), 19. Kanwar Lake (Phartiyal et al., 2024).

Magnetic concentration parameters (χ_{lf}, χ_{ARM}, SIRM) showed a modest increasing trend with enhanced variability, while grain-size indicators (χ_{ARM}/SIRM, χ_{ARM}/χlf) and moderate χ_{fd}% suggested finer magnetic grains and SP-coarse admixtures (Dearing, 1999). Magnetic mineralogy remains dominated by ferrimagnetic assemblages, though intermittent high-coercive antiferromagnetic substances suggest fluctuating sediment sources. End-members shifted toward finer-grained (EM1, EM2) dominance, with reduced EM3; TOC increased, reflecting better preservation/productivity, and declining TOC/TN ratios indicated greater input of aquatic organic matter. Two short, dry episodes were marked by coarser magnetic grain size, lower χfd%, elevated EM3, reduced TOC, and high-coercivity magnetic minerals, as evidenced by low S-ratios and high HIRM.

Sedimentary archives across the CGP and adjoining regions document significant mid- to late Holocene climatic variability. At Nawabganj Lake, a prominent calcrete layer records intense aridity between ~5000 and 4600 cal yrs. BP, with peak dryness precisely coinciding with the globally recognized 4.2 ka Meghalayan drought event (Farooqui et al., 2023). In contrast, Jalesar Lake preserves a diverse arboreal assemblages between 4700 and 3200 cal yrs. BP, reflecting a warm-humid interval superimposed on this broader arid backdrop (Trivedi et al., 2013). Similarly, Chandrika Devi Lake documents enhanced fluvial activity during 5900–4100 cal yrs. BP, linked to stronger monsoon winds and indicated by EM4 dominance alongside δ^{13}Corg values characteristic of C_3 vegetation (Sengupta et al., 2024). This wet phase extended through 4100–3000 cal yrs. BP, corroborated by high coarse silt fractions at Lilaur Lake (3730–3070 cal yrs. BP; Singh et al., 2022) and regional evidence of ISM intensification between 4800 and 2000 cal yrs. BP (Chauhan et al., 2015).

From the Uttarakhand Himalaya, Rawat et al. (2021) reconstructed high lake levels and enhanced productivity at Bednikund Lake during wet phases (~5930–3950, ~3380–2830, ~2610–1860, ~1050–760, ~580–500, ~320 cal yrs. BP to present), marked by increasing EM1, TOC, TN, and decreasing δ^{13}Corg values. Intervening dry intervals (~3950–3380, ~2830–2610, ~1860–1050, ~760–580, ~500–320 cal yrs. BP) show reduced TOC/TN, elevated magnetic concentrations, coarse EM2/EM3 inputs, and enriched δ^{13}Corg, indicating shallower lakes.

Beyond the CGP, Lonar Lake (Central India) records prolonged drought (4600–3900 cal yrs. BP; Prasad et al., 2014), contrasting with Nal Lake's (Central Gujarat) wettest phase (4800–3000 cal yrs. BP) followed by gradual aridification (Prasad et al., 1997; Quamar et al., 2024). Kothiyakhad (Gujarat; 3660–3400 cal yrs. BP) suggests weak ISM, compensated by winter precipitation (Prasad et al., 2007).

5.3.3. HK-3 (2920–2332 cal yrs. BP): Weakened Monsoon

Between 2920 and 2332 cal yrs. BP, coarser magnetic grains were dominant alongside mixed low- and high-coercivity minerals, with elevated coarse end-member contributions indicating increased detrital input. This phase aligns with regional evidence of weakened ISM, as documented by Phartiyal et al. (2024) in the form of fine-grained sedimentation (~3000–2300 cal yrs. BP) at Kanwar Wetland, reflecting reduced monsoon runoff. Sengupta et al. (2024) and Tripathi et al. (2017) report persistent dry conditions at Chandrika Devi Lake (deposition of clay/silt; EM1) and Karela Jheel (high Iph) since ~3000 cal yrs. BP, indicating sustained low lake levels. Beyond the CGP, rising δ^{18}Ocarb values in the Higher Himalaya from ~2700 cal yrs. BP (Mishra et al., 2015) and a semi-humid to semi-arid transition in the Thar Desert (Sinha et al., 2006) confirm the broader regional decline in monsoon intensity.

5.3.4. HK-4 (2332–1767 cal yrs. BP): Fluctuating Moisture with increased Productivity

Between 2332 and 1767 cal yrs. BP, moderate magnetic concentrations and dominant ferrimagnetic mineralogy coexisted with finer magnetic grains and fluctuating EM1/EM2–EM3 proportions, indicating variable sediment supply and depositional energy. Rising TOC with stable high TOC/TN ratios suggests enhanced lake productivity alongside sustained terrestrial organic input, reflecting episodic monsoon intensification. This aligns with CGP records documenting a moist-warm phase (~2500–1800 cal yrs. BP) marked by C_3 vegetation dominance, increased EM2, stable Rb/Sr ratios, and declining δ^{13}Corg values (Sengupta et al., 2024).

5.3.5. HK-5 (1767–1360 cal yrs. BP): Reduced Lake Levels and Drying Trend

Between 1767 and 1360 cal yrs. BP, coarse-grained deposition dominated (EM3 with episodic EM4 ~ 1500 cal yrs. BP), indicated by coarser magnetic grains, low χ_{fd}%, and declining TOC and TOC/TN ratios reflecting reduced lake levels and moisture availability. This phase aligns well with records of the weakening of the regional monsoon. At Karela Jheel, Chauhan et al. (2015) documented a reduction in monsoon precipitation beginning after ~2000 cal yrs. BP, a trend mirrored in the Chandrika Devi Lake record, where Sengupta et al. (2024) identified a weak monsoon interval between 1550 and 1100 cal yrs. BP. Broader evidence from Central India also indicates a prolonged drought spanning ~2000–600 cal yrs. BP (Prasad et al., 2014), which aligns with the reduced lake levels and coarse sediment influx evident in the present record.

5.3.6. HK-6 (1360–613 cal yrs. BP): High Variability and Medieval Warm Period Signals

Between 1360 and 613 cal yrs. BP, the sediment record documents heightened depositional variability. Magnetic concentration parameters (χ_{lf} and χ_{ARM}) remain moderately high, while SIRM reaches its peak values, signifying pulses of enhanced influx of magnetic minerals into the lake system. Magnetic grain-size indicators and sediment end-member distributions fluctuated between fine and coarse fractions, reflecting variable sediment transport and depositional energy. TOC increased gradually while TOC/TN ratios remained elevated, indicating enhanced lake productivity with persistent terrestrial inputs. Collectively, the data suggest an initial dry interval followed by a transition to wetter conditions after ~900 cal yrs. BP. Elevated $\delta^{18}O_{carb}$ (‰) values between ~1400 and 1100 cal yrs. BP from Lonar (Prasad et al., 2014), Ropan Chappra (Singh et al., 2015), and Kotla Dahar (Dixit et al., 2014) point to drier conditions, possibly linked to the Dark Ages Cold Period (DACP) (Misra et al., 2019). This was followed by a wetter phase between ~1050 and 750 cal yrs. BP as reported by Singh et al. (2015) based on depleted δ^{18}O values, suggesting intensified ISM activity. The latter interval aligns with the Medieval Warm Period (MWP), a period of enhanced precipitation, elevated lake levels, and increased productivity in several Indian records (Rawat et al., 2021). Taken together, the proxies from this interval indicate that the HK section record responded strongly to Late Holocene monsoon variability, first reflecting the DACP-associated dry phase, then transitioning into a wetter regime consistent with the MWP across South Asia.

5.3.7. 613–298 Cal yrs. BP: Transition to Low-Energy Deposition under Reduced Monsoon Forcing

Moderate magnetic concentrations characterize the interval, and fluctuating S-ratio values suggest a mixed magnetic mineral assemblage. Magnetic grain-size parameters and sediment end-members (EM1, EM2 dominance with episodic EM3) indicate finer grains and low-energy deposition punctuated by intermittent higher-energy inputs. TOC values remain steady, but variable, while lower TOC/TN ratios suggest shifts in vegetation cover, enhanced aquatic productivity, or early diagenetic alteration within the lake sediments. Trivedi et al. (2013) reported a transition to warmer, drier conditions since ~1200 cal yrs. BP in north-central India, inferred from a decline in arboreal pollen linked to a weakening of the ISM. Broadly, most palaeoclimate records from across the Indian subcontinent document a progressive decrease in ISM intensity during the late Holocene, following the mid-Holocene

maximum and culminating in the 4.2 ka event (Berkelhammer et al., 2012; Kathayat et al., 2017).

In southern India, palaeomonsoon archives indicate a generally drier mid-Holocene (Sukumar et al., 1993), but a shift to wetter intervals during the late Holocene, marked by increased sedimentation and lake productivity (Resmi et al., 2022). Comparable weakening of ISM strength during these intervals is also observed in continental Oman speleothems (Fleitmann et al., 2007), marine records from the Arabian Sea (Gupta et al., 2005), and sediments from the Bay of Bengal (Ponton et al., 2012), and peninsular India (Sandeep et al., 2017), pointing to a broad regional signal driven by a combination of declining Northern Hemisphere summer insolation and internal climate system feedbacks. Nevertheless, vegetation and sedimentary records from the Gangetic Plains and northwestern India (Prasad and Enzel, 2006; Saxena et al., 2015; Saxena and Trivedi, 2017) reveal spatially heterogeneous hydroclimatic conditions, suggesting that local precipitation variability was shaped not only by large-scale monsoon forcing but also by differential moisture sources, proxy-specific sensitivities, and catchment-scale processes.

5.4. *Regional Coherence and Temporal Heterogeneity of ISM during the Holocene in the CGP*

To identify regionally consistent palaeoclimatic events and reconstruct the evolution of the ISM during the mid- to late-Holocene, our multi-proxy HK record was correlated with selected terrestrial, marine, and ice-core archives. Establishing such cross-system correlations is essential for evaluating whether climate changes occurred synchronously across regions or if there were temporary offsets. Because previous studies have emphasized the influence of ocean-atmosphere processes on the ISM variability (Ashok et al., 2001; Goswami et al., 2006; Hrudya et al., 2021; Nair et al., 2018; Sabeerali et al., 2019; Saji et al., 1999), our correlation framework integrates magnetic, sedimentary, and C—N data from the HK with $\delta^{18}O$ from the NGRIP (North Greenland Ice Core Project Members, 2004), ^{10}Be flux from GISP2 (Greenland Ice Sheet Project 2, Finkel and Nishiizumi, 1997), *G. bulloides* $\delta^{18}O$ from the western Arabian Sea (Gupta et al., 2003), mean grain size data from the Kanwar Wetland in the CGP (Phartiyal et al., 2024), and June–July-August (JJA) insolation (Laskar et al., 2004). These datasets are illustrated in Fig. 8 together to allow evaluation of the relative influence of ocean-atmosphere forcing and solar-driven variability on ISM behaviour.

The integrated HK multi-proxy record reveals a dynamic depositional regime tightly coupled to fluctuations in ISM strength. High-resolution grain-size distributions, mineral magnetic characteristics and the C—N record collectively indicate the sedimentation patterns across the mid to late Holocene reflects shifts in monsoon strength and hydrodynamic conditions within the CGP (Fig. 8). Wet phases were characterized by an abundance of finer EMs (1–2), lower SIRM/χ_{lf} and high χ_{ARM}/SIRM values, and elevated TOC percentages. These indicators

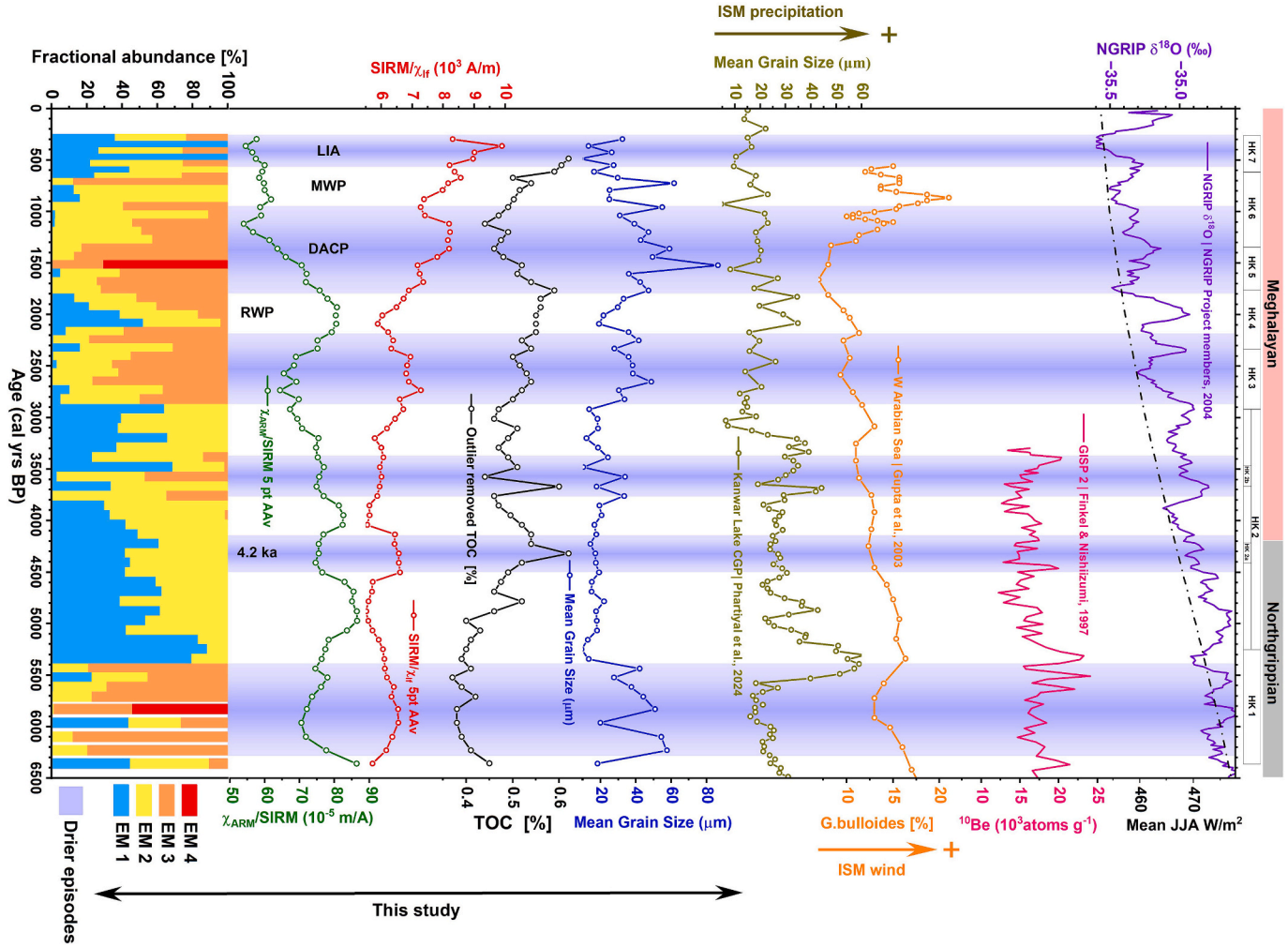

Fig. 8. Correlation between the Hulas Khera sediment record (End Member, Mean Grain Size, SIRM/χ_{lf} and χ_{ARM}/χ_{lf}) and the Mean Grain Size record from Kanwar Wetland, CGP (Phartiyal et al., 2024), *G. bulloides* $\delta^{18}O$ records from the western Arabian Sea (Gupta et al., 2003), ^{10}Be flux record from Greenland Ice Sheet Project 2 (Finkel and Nishiizumi, 1997), $\delta^{18}O$ NGRIP ice core records (North Greenland Ice Core Project members, 2004), Mean JJA insolation record (Laskar et al., 2004).

suggest increased catchment runoff and sediment flux into the lake, reflecting intensified ISM during wet events around 5400 to 4600, 4000, 3300, 2000, and 800 cal yrs. BP. Conversely, dry phases were characterized by a coarser magnetic grain size (high SIRM/χ_{lf}, low χ_{ARM}/χ_{lf} and χ_{ARM}/SIRM); reduced mineral magnetic concentrations, dominance of coarser EM3 and EM4 fractions, and low TOC values. These are consistent with lake-level reduction, shoreline erosion, and drought-driven catchment destabilization, occurring during ~6300–5400, ~4300, ~3600, ~2800–2200, ~1800–900, and ~ 600–300 cal yrs. BP. Strikingly, the prolonged drought intervals and monsoon minima recorded in the HK record show strong temporal coherence with the Kanwar Wetland record from CGP (Phartiyal et al., 2024), which documents analogous dry events at 6100–5300, 4300–4200, 3800, 2800, 1800–900, and 300 cal yrs. BP. Synchrony with the western Arabian Sea records (Gupta et al., 2003) further supports the interpretation that episodes of weak ISM phases correspond to reduced wind strength and diminished upwelling intensity (Fig. 8). Interestingly, the TOC values at approximately ~4300 and ~ 3600 cal yrs. BP are relatively high in comparison to other arid intervals. One plausible reason could be reduced clastic dilution. In Lake Malawi, a comparable pattern was observed, with high TOC variability attributed to reduced minerogenic dilution rather than increased organic productivity (Scholz et al., 2007). Additionally, the lake's nutrient cycling may have been altered by protracted drought, which may have facilitated internal nutrient recycling and localized plankton productivity (e.g., Catalan et al., 2024). Consequently, the elevated TOC during these otherwise arid intervals may result from a combination of reduced detrital input (higher relative TOC values) and increased in-lake productivity under shallower, stagnant conditions, suggesting Karela Lake likely underwent shrinkage during these periods.

The early Holocene strengthening of the ISM (~11–7 ka) has been attributed to the progressive northward migration of the summer ITCZ, which enhanced convection and moisture advection (Demske et al., 2009; Fleitmann et al., 2003; Gupta et al., 2003; Prasad et al., 2014; Wünnemann et al., 2010). However, after ~7 ka, the ISM gradually weakened under declining Northern Hemisphere summer insolation (Fleitmann et al., 2007; Haug et al., 2001), triggering a southward migration of ITCZ and recurring dry phases (Demske et al., 2009; Gupta et al., 2003; Overpeck et al., 1996). A decline in summer insolation weakened the land-sea thermal gradient, reducing the northward shift of the ITCZ and monsoon rainfall into the Arabian Peninsula (Fleitmann et al., 2003). In tropical South America, declining Ti concentrations (Haug et al., 2001) correspond to long-term southward migration of the ITCZ and reduced summer precipitation under insolation forcing. While in the Arabian Sea, reduced SST and productivity signal enhanced evaporation and reduced monsoon convection (~6400 cal yrs. BP; Saraswat et al., 2016). Comparable aridification signals are observed in Lonar Lake (Sarkar et al., 2015) and Himalayan Lake records (Rawat et al., 2015). Late Holocene ISM decline is similarly well documented in peninsular India (Shantisagar Lake, Sandeep et al., 2017; archaeological evidence in Gupta et al., 2006), in marine sediments from the western Indian margin (Thamban et al., 2007), and in Bay of Bengal archives (Giosan et al., 2017; Kawsar et al., 2023; Ponton et al., 2012). Lake and speleothem studies (Nag et al., 2023; Prasad et al., 2014; Sinha et al., 2011) also confirm late Holocene aridification, which occurred under declining insolation. Geochemical and sedimentological evidence from SW China indicates peak ISM intensity between 7500 and 5200 cal yrs. BP (Cui et al., 2022), coinciding with anomalous tropical Indian Ocean warming under a positive Indian Ocean Basin Mode and IOD phase (Sun et al., 2019). Such anomalous SSTs have been shown to strengthen convection and precipitation (Trenberth and Shea, 2005). However, time lags and regional differences in response occur across the Indian Ocean basins (Roxy et al., 2013).

5.5. Climate Oscillation in the CGP: Links to Solar Forcing and North Atlantic Processes

Millennial-scale cold intervals identified by peaks in North Atlantic ice-rafted debris (HSG%) records, reflecting changes in ocean circulation and climate (Bond et al., 1997), are termed Bond Events. These events are well captured in marine archives, which often record synchronous responses, whereas continental proxy records are generally limited in their ability to resolve such high-frequency perturbations. The Holocene has seen several multi-decadal to centennial cold events, though their mechanisms remain poorly understood (Banerji and Padmalal, 2022; Wanner et al., 2015). Detailed global climate perturbation records from Greenland and Antarctic ice cores have been compared with tropical archives to elucidate these events (Gupta et al., 2003; Phartiyal et al., 2024; Staubwasser et al., 2002). Gupta et al. (2003) demonstrated that abrupt Holocene weakening of ISM winds coincided with Bond Events (Bond et al., 2001; Bond et al., 1997). These intervals correspond to high-latitude cooling pulses, often driven by meltwater–induced disruptions of the Atlantic Meridional Overturning Circulation (AMOC) and related atmospheric changes over Greenland (Bond et al., 2001; Rasmussen et al., 2007). The role of external forcing remains debated. Some studies suggest that solar output variations directly triggered monsoon weakening (Shindell et al., 2001), while others propose indirect modulation via internal ocean–atmosphere feedbacks (Gupta et al., 2003; Neff et al., 2001). Regardless, it is evident that solar-induced Bond events influenced Holocene monsoon variability in South Asia (Fleitmann et al., 2003).

The correlation between our HK sediment data, monsoon minima in the Kanwar wetland, and reduced Arabian Sea upwelling. Millennial-scale North Atlantic drift ice proxy peaks strongly suggest reduced ISM precipitation in the CGP during the studied time (Fig. 8). Gupta et al. (2003) found that abrupt Holocene weakening of ISM winds coincides with millennial-scale North Atlantic drift ice and hydrographic changes, shown by HSG% records in deep-sea sediments (Bond et al., 1997, 2001). Centennial-scale HSG% oscillations (200–500 yr) coupled with cosmogenic radionuclides reflect reduced solar output and Northern Hemisphere cooling, while millennial (1500 yr) HSG% peaks indicate solar-driven North Atlantic cooling during the Holocene (Bond et al., 1997, 2001). Phartiyal et al. (2024) suggested that the ~1492-year ISM cycles in the Kanwar Lake record reflect combined external (solar) and internal (AMOC) forcing during the Holocene, as this cycle also appears in low-latitude monsoons, such as the ~1450-year Mg cycles in the Western Arabian Sea (Sirocko et al., 1996). Abrupt weakening of the ISM during North Atlantic cooling intervals is consistently reflected across South and East Asian monsoon proxy records (Gupta et al., 2003; Phartiyal et al., 2024; Wang et al., 2005). High-resolution oxygen isotope data from Sahiya Cave speleothems record abrupt ISM shifts over the past 6000 cal yrs. BP that closely track Northern Hemisphere temperature fluctuations (Kathayat et al., 2017). Notably, the arid phase identified between 6600 and 6000 cal yrs. BP in Sambhar Playa (Sinha et al., 2006) and Nal Lake (Prasad et al., 1997) highlights a strong teleconnection between high-latitude cooling and ISM weakening (Banerji and Padmalal, 2022). In contrast, other regional records reveal a different climate trajectory. For example, a warm and humid phase between 6900 and 4800 cal yrs. BP in Tso Kar Lake (Demske et al., 2009) likely reflects the persistence of the Holocene climate optimum. These contrasting signals underscore the complexity of monsoon responses, where large-scale Bond Events may be superimposed on regionally variable hydroclimatic trends.

Multiple lines of evidence highlight the abrupt weakening of the ISM around the ~4200 yr event, a globally recognized climatic perturbation. Marine archives from the Arabian Sea (Staubwasser et al., 2002), speleothem records from NE India (Berkelhammer et al., 2012), and lacustrine records (Dixit et al., 2014; Prasad et al., 2014; Sarkar et al., 2015) consistently document pronounced aridity during this interval. Between 3000 and 2000 cal yrs. BP, marine, and continental records

documented declining ISM strength (Lückge et al., 2001; Srivastava et al., 2017). Sinha et al. (2018) reported abrupt ISM weakening between ~3180 and 1720 cal yr BP based on Kadapa Cave speleothem data, suggesting that reduced Northern Hemisphere summer insolation drove a southward shift in the ITCZ and reduced monsoon activity across India. Lonar Lake sediments further reveal centennial-scale weak-monsoon episodes between 2000 and 600 cal yrs. BP (Prasad et al., 2014). More recently, the Little Ice Age (650–100 cal yrs. BP) was characterized by glacier advances, cooler winters, and declining harvests across the Northern Hemisphere (Lamb, 1965). These episodes of ISM weakening underscore the critical role of ITCZ dynamics in modulating monsoon variability. During periods of sustained episodes of NH cooling, a strengthened meridional temperature gradient forced the ITCZ southward, resulting in protracted break-monsoon spells over the Indian subcontinent. Such teleconnections reveal how high-latitude forcing, transmitted through coupled ocean–atmosphere circulation, shaped millennial-to-centennial-scale hydroclimate variability in the ISM domain during the Holocene.

6. Conclusions

This study examines a sediment profile from the HK section in the CGP using a multi-proxy approach to reconstruct past climatic conditions and lake-level fluctuations since ~6350 cal yrs. BP.

- Variations in detrital input reflect catchment erosion linked to shifts in rainfall patterns, identifying precipitation as the primary driver of magnetic property changes in the HK sediments and dividing the section to seven climatic zones-HK 1 (6358–5251 cal yrs. BP), HK 2 (5251–2920 cal yrs. BP), HK 3 (2920–2332 cal yrs. BP), HK 4 (2332–1767 cal yrs. BP), HK 5 (1767–1361 cal yrs. BP), HK 6 (1361–613.5 cal yrs. BP) and HK 7 (613.5–298 cal yrs. BP).
- Predominantly floodplain deposition between ~5400 and 2900 cal yrs. BP, driven by suspension settling.
- Between 6350 and 5400, 4600 and 4100, 3800, 2800 and 2300, 1800 and 900, and around 500 and 300 cal yrs. BP, the CGP experienced extended drought periods due to monsoon minima (ISM).
- Enhanced catchment runoff and sediment flux into the lake around 5400 to 4600, 4000, 3300, 2000, and 800 cal yrs. BP, reflecting wet phases during intensified ISM.
- Abrupt shifts in ISM strength recorded in the HK profile correspond to known monsoon minima during the Little Ice Age, and the Dark Age Cold Period.

CRediT authorship contribution statement

Arvind Tiwari: Writing – review & editing, Writing – original draft, Validation, Software, Methodology, Formal analysis, Data curation. **Binita Phartiyal:** Writing – review & editing, Writing – original draft, Visualization, Validation, Supervision, Resources, Project administration, Methodology, Data curation, Conceptualization. **M.C. Manoj:** Writing – review & editing, Validation, Methodology, Data curation. **Masud Kawsar:** Writing – review & editing, Validation, Software, Methodology. **K. Prasanna:** Writing – review & editing, Validation, Software, Methodology, Data curation. **Rajveer Sharma:** Writing – review & editing, Software, Methodology. **Pankaj Kumar:** Writing – review & editing, Validation, Methodology, Data curation. **Anupam Sharma:** Writing – review & editing, Resources, Project administration.

Declaration of competing interest

The authors declare that they have no known competing financial interests or personal relationships that could have appeared to influence the work reported in this paper.

Acknowledgments

This work was performed under the auspices of Birbal Sahni Institute of Palaeosciences, Lucknow, India (BSIP/RDCC/52/25-26) as a part of the QLDP Mega Lake Coring project. Authors are thankful to SAIF BSIP, Lucknow, and IUAC for extending the AMS facility for 14C funded by the Ministry of Earth Science (MoES), Govt. of India, with reference numbers MoES/16/07/11(i)-RDEAS and MoES/P.O.(Seismic)8(09)-Geochron/2012. AT gratefully acknowledges UGC (426/CSIR-UGC NET JUNE 2019) for financial support in the form of JRF and SRF. Dr. Debarati Nag and Mr. Shirish Verma are thanked for their help during field work.

Appendix A. Supplementary data

Supplementary data to this article can be found online at https://doi.org/10.1016/j.palaeo.2026.113551.

Data availability

The authors confirm that all data necessary for supporting the scientific findings of this paper have been provided.

References

Agarwal, A.K., Rizvi, M.H., Singh, I.B., Kumar, A., Chandra, S., 1992. Carbonate deposits in Ganga Plain. In: Singh, I.B. (Ed.), Gangetic Plain: Terra Incognita. Geology Department, Lucknow University, pp. 35^43.

Agnihotri, R., Dutta, K., Bhushan, R., Somayajulu, B.L.K., 2002. Evidence for solar forcing on the Indian monsoon during the last millennium. Earth Planet. Sci. Lett. 198, 521–527. https://doi.org/10.1016/S0012-821X(02)00530-7.

Aitchison, J., 1986. The Statistical Analysis of Compositional Data. Chapham and Hall, London, New York.

Anderson, N.J., Rippey, B., 1988. Diagenesis of magnetic minerals in the recent sediments of a eutrophic lake. Limnol. Oceanogr. 33, 1476–1492. https://doi.org/10.4319/lo.1988.33.6part2.1476.

Andreola, F., Castellini, E., Manfredini, T., Romagnoli, M., 2004. The role of sodium hexametaphosphate in the dissolution process of kaolinite and kaolin. J. Eur. Ceram. Soc. 24, 2113–2124. https://doi.org/10.1016/S0955-2219(03)00366-2.

Ashok, K., Guan, Z., Yamagata, T., 2001. Impact of the Indian Ocean dipole on the relationship between the Indian monsoon rainfall and ENSO. Geophys. Res. Lett. 28, 4499–4502. https://doi.org/10.1029/2001GL013294.

Banerji, U.S., Padmalal, D., 2022. 12 - Bond events and monsoon variability during Holocene—Evidence from marine and continental archives. In: Kumaran, N., Damodara, P. (Eds.), Holocene Climate Change and Environment. Elsevier, pp. 293–339. https://doi.org/10.1016/B978-0-323-90085-0.00016-4.

Basavaiah, N., Seetharamaiah, J., Appel, E., Juyal, N., Prasad, S., Kakani, N.R., Khadkikar, A., Nowaczyk, N., Brauer, A., 2021. Holocene Environmental Magnetic Records of Indian Monsoon Fluctuations, pp. 229–246. https://doi.org/10.1016/B978-0-323-90085-0.00004-8.

Battarbee, R.W., Jones, V.J., Flower, R.J., Cameron, N.G., Bennion, H., 2001. Diatoms. In: Smol, J.P., Birks, H.J.B., Last, W.M. (Eds.), Tracking Environmnental Change Using Lake Sediments. Volume 3: Terrestrial, Algal and Siliceous Indicators. Kluwer Academic Publishers, Dordrecht, pp. 155–202.

Berkelhammer, M., Sinha, A., Stott, L., Cheng, H., Pausata, F.S.R., Yoshimura, K., 2012. An abrupt shift in the Indian Monsoon 4000 years ago. In: Climates, Landscapes, and Civilizations. American Geophysical Union (AGU), pp. 75–88. https://doi.org/10.1029/2012GM001207.

Bird, B.W., Polisar, P.J., Lei, Y., Thompson, L.G., Yao, T., Finney, B.P., Bain, D.J., Pompeani, D.P., Steinman, B.A., 2014. A Tibetan lake sediment record of Holocene Indian summer monsoon variability. Earth Planet. Sci. Lett. 399, 92–102. https://doi.org/10.1016/j.epsl.2014.05.017.

Blott, S.J., Pye, K., 2001. GRADISTAT: a grain size distribution and statistics package for the analysis of unconsolidated sediments. Earth Surf. Process. Landf. 26, 1237–1248. https://doi.org/10.1002/esp.261.

Bond, G., Showers, W., Cheseby, M., Lotti, R., Almasi, P., deMenocal, P., Priore, P., Cullen, H., Hajdas, I., Bonani, G., 1997. A pervasive millennial-scale cycle in North Atlantic Holocene and glacial climates. Science 278, 1257–1266. https://doi.org/10.1126/science.278.5341.1257.

Bond, G., Kromer, B., Beer, J., Muscheler, R., Evans, M.N., Showers, W., Hoffmann, S., Lotti-Bond, R., Hajdas, I., Bonani, G., 2001. Persistent solar influence on North Atlantic climate during the Holocene. Science 294, 2130–2136. https://doi.org/10.1126/science.1065680.

Bronk Ramsey, C., 2021. OxCal v. 4.4. 4 [software]. URL: https://c14.arch.ox.ac.uk/oxcal.html.

Catalan, J., Monteoliva, A.P., Vega, J.C., Domínguez, A., Negro, A.I., Alonso, R., Garcés, B.V., Batalla, M., García-Gómez, H., Leira, M., Nuño, C., Pahissa, J., Peg, M., Pla-Rabés, S., Roblas, N., Vargas, J.L., Toro, M., 2024. Reduced precipitation can

induce ecosystem regime shifts in lakes by increasing internal nutrient recycling. Sci. Rep. 14, 12408. https://doi.org/10.1038/s41598-024-62810-9.
Chauhan, M.S., Pokharia, A.K., Srivastava, R.K., 2015. Late Quaternary vegetation history, climatic variability and human activity in the Central Ganga Plain, deduced by pollen proxy records from Karela Jheel, India. Quat. Int. 371, 144–156. https://doi.org/10.1016/j.quaint.2015.03.025.
Chauhan, M.S., Pokharia, A.K., Bhandari, Y., 2018. Quaternary vegetation, climate, farming and human habitation in the Ganga plain, based on pollen and macro-botanical remains from lakes and archaeological sites. Indian J. Archaeol. 3, 1–65.
Cui, K., Wang, Yongbo, Liu, X., Shen, J., Wang, Yong, 2022. Holocene variation in the Indian Summer Monsoon modulated by the tropical Indian Ocean Sea-surface temperature mode. CATENA 215, 106302. https://doi.org/10.1016/j.catena.2022.106302.
Dearing, J.A., 1999. Holocene environmental change from magnetic proxies in lake sediments. In: Maher, B.A., Thompson, R. (Eds.), Quaternary Climates, Environments and Magnetism. Cambridge University Press, Cambridge, pp. 231–278. https://doi.org/10.1017/CBO9780511535635.008.
Dearing, J.A., Bird, P.M., Dann, R.J.L., Benjamin, S.F., 1997. Secondary ferrimagnetic minerals in Welsh soils: a comparison of mineral magnetic detection methods and implications for mineral formation. Geophys. J. Int. 130, 727–736. https://doi.org/10.1111/j.1365-246X.1997.tb01867.x.
Demske, D., Tarasov, P.E., Wünnemann, B., Riedel, F., 2009. Late glacial and Holocene vegetation, Indian monsoon and westerly circulation in the Trans-Himalaya recorded in the lacustrine pollen sequence from Tso Kar, Ladakh, NW India. Palaeogeogr. Palaeoclimatol. Palaeoecol. 279, 172–185. https://doi.org/10.1016/j.palaeo.2009.05.008.
Dietze, E., Dietze, M., 2019. Grain-size distribution unmixing using the R package EMMAgeo. E&G Quatern. Sci. J. 68, 29–46. https://doi.org/10.5194/egqsj-68-29-2019.
Dietze, E., Hartmann, K., Diekmann, B., Ijmker, J., Lehmkuhl, F., Opitz, S., Stauch, G., Wünnemann, B., Borchers, A., 2012. An end-member algorithm for deciphering modern detrital processes from Lake sediments of Lake Donggi Cona, NE Tibetan Plateau, China. Sediment. Geol. 243–244, 169–180. https://doi.org/10.1016/j.sedgeo.2011.09.014.
Dietze, M., Schulte, P., Dietze, E., 2022. Application of end-member modelling to grain-size data: Constraints and limitations. Sedimentology 69, 845–863. https://doi.org/10.1111/sed.12929.
Dixit, Y., Hodell, D.A., Petrie, C.A., 2014. Abrupt weakening of the summer monsoon in Northwest India ~4100 yr ago. Geology 42, 339–342. https://doi.org/10.1130/G35236.1.
Evans, M.E., Heller, F., 2003. Environmental Magnetism: Principles and Applications of Enviromagnetics, International Geophysics Series. Academic Press, Amsterdam, Boston.
Farooqui, A., Khan, S., Agnihotri, R., Phartiyal, B., Shukla, S., 2023. Monitoring hydroecology and climatic variability since ~4.6 ka from palynological, sedimentological and environmental perspectives in an Ox-bow lake, Central Ganga Plain, India. Holocene 33, 1272–1288. https://doi.org/10.1177/09596836231183067.
Finkel, R.C., Nishiizumi, K., 1997. Beryllium 10 concentrations in the Greenland ice sheet project 2 ice core from 3–40 ka. J. Geophys. Res. Ocean. 102, 26699–26706. https://doi.org/10.1029/97JC01282.
Fleitmann, D., Burns, S.J., Mudelsee, M., Neff, U., Kramers, J., Mangini, A., Matter, A., 2003. Holocene forcing of the Indian Monsoon recorded in a stalagmite from southern Oman. Science 300, 1737–1739. https://doi.org/10.1126/science.1083130.
Fleitmann, D., Burns, S.J., Mangini, A., Mudelsee, M., Kramers, J., Villa, I., Neff, U., Al-Subbary, A.A., Buettner, A., Hippler, D., Matter, A., 2007. Holocene ITCZ and Indian monsoon dynamics recorded in stalagmites from Oman and Yemen (Socotra). Quat. Sci. Rev. 26, 170–188. https://doi.org/10.1016/j.quascirev.2006.04.012.
Gadgil, S., 2018. The monsoon system: Land–sea breeze or the ITCZ? J. Earth Syst. Sci. 127, 1. https://doi.org/10.1007/s12040-017-0916-x.
Gautam, P., Blaha, U., Appel, E., Neupane, G., 2004. Environmental magnetic approach towards the quantification of pollution in Kathmandu urban area, Nepal. Phys. Chem. Earth 29, 973–984. https://doi.org/10.1016/j.pce.2004.02.001.
Giosan, L., Ponton, C., Usman, M., Blusztajn, J., Fuller, D.Q., Galy, V., Haghipour, N., Johnson, J.E., McIntyre, C., Wacker, L., Eglinton, T.I., 2017. Short communication: massive erosion in monsoonal Central India linked to late Holocene land cover degradation. Earth Surf. Dyn. 5, 781–789. https://doi.org/10.5194/esurf-5-781-2017.
Goswami, B.N., Madhusoodanan, M.S., Neema, C.P., Sengupta, D., 2006. A physical mechanism for North Atlantic SST influence on the Indian summer monsoon. Geophys. Res. Lett. 33. https://doi.org/10.1029/2005GL024803.
Grimm, E.C., 1987. CONISS: a FORTRAN 77 program for stratigraphically constrained cluster analysis by the method of incremental sum of squares. Comput. Geosci. 13, 13–35. https://doi.org/10.1016/0098-3004(87)90022-7.
Grimm, E.C., 1990. TILIA and TILIA.GRAPH, PC spreadsheet and graphics software for pollen data. In: INQUA. Working Group on Data-handling Methods Newsletter 4, pp. 5–7.
Gupta, A.K., Anderson, D.M., Overpeck, J.T., 2003. Abrupt changes in the Asian southwest monsoon during the Holocene and their links to the North Atlantic Ocean. Nature 421, 354–357. https://doi.org/10.1038/nature01340.
Gupta, A.K., Das, M., Anderson, D.M., 2005. Solar influence on the Indian summer monsoon during the Holocene. Geophys. Res. Lett. 32. https://doi.org/10.1029/2005GL022685.
Gupta, A.K., Anderson, D.M., Pandey, D.N., Singhvi, A.K., 2006. Adaptation and human migration, and evidence of agriculture coincident with changes in the Indian summer monsoon during the Holocene. Curr. Sci. 90, 1082–1090.
Harris, I., Osborn, T.J., Jones, P., Lister, D., 2020. Version 4 of the CRU TS monthly high-resolution gridded multivariate climate dataset. Sci. Data 7. https://doi.org/10.1038/s41597-020-0453-3.
Haslett, J., Parnell, A., 2008. A simple monotone process with application to radiocarbon-dated depth chronologies. J. R. Stat. Soc.: Ser. C: Appl. Stat. 57, 399–418. https://doi.org/10.1111/j.1467-9876.2008.00623.x.
Haug, G.H., Hughen, K.A., Sigman, D.M., Peterson, L.C., Röhl, U., 2001. Southward migration of the intertropical convergence zone through the Holocene. Science 293, 1304–1308. https://doi.org/10.1126/science.1059725.
Hrouda, F., 2011. Models of frequency-dependent susceptibility of rocks and soils revisited and broadened. Geophys. J. Int. 187, 1259–1269. https://doi.org/10.1111/j.1365-246X.2011.05227.x.
Hrudya, P.P.V.H., Varikoden, H., Vishnu, R.N., 2021. Changes in the relationship between Indian Ocean dipole and Indian summer monsoon rainfall in early and recent multidecadal epochs during different phases of monsoon. Int. J. Climatol. 41, E305–E318. https://doi.org/10.1002/joc.6685.
Jha, D.K., Vaishnav, H.K., Roy, N., 2024. Late Quaternary human-environment relationship in the Ganga Plain, India. Quat. Int. 680, 1–16. https://doi.org/10.1016/j.quaint.2024.01.002.
Kathayat, G., Cheng, H., Sinha, A., Yi, L., Li, X., Zhang, H., Li, H., Ning, Y., Edwards, R.L., 2017. The Indian monsoon variability and civilization changes in the Indian subcontinent. Sci. Adv. 3, e1701296. https://doi.org/10.1126/sciadv.1701296.
Kawsar, M., Manoj, M.C., Weber, M.E., 2023. Reconstructing dynamics of northern and southern sourced bottom waters during the last 200 ka using sortable silt records in the lower Bengal Fan. Z. Dtsch. Ges. Geowiss. 651–673. https://doi.org/10.1127/zdgg/2022/0318.
Kim, B., Kodama, K.P., Moeller, R.E., 2005. Bacterial magnetite produced in water column dominates lake sediment mineral magnetism: Lake Ely, USA. Geophys. J. Int. 163, 26–37. https://doi.org/10.1111/j.1365-246X.2005.02735.x.
King, J., Banerjee, S.K., Marvin, J., Özdemir, Ö., 1982. A comparison of different magnetic methods for determining the relative grain size of magnetite in natural materials: some results from lake sediments. Earth Planet. Sci. Lett. 59, 404–419. https://doi.org/10.1016/0012-821X(82)90142-X.
Kumar, M., Saikia, K., Agrawal, S., Ghosh, R., Ali, S.N., Arif, Md., Singh, D.S., Sharma, A., Phartiyal, B., Bajpai, S., 2022. Climatic control on the C_3 anδ C_4 plant abundance during the late Pleistocene – Holocene in the northern Gangetic Plain, India. Palaeogeogr. Palaeoclimatol. Palaeoecol. 591, 110890. https://doi.org/10.1016/j.palaeo.2022.110890.
Lamb, H.H., 1965. The early medieval warm epoch and its sequel. Palaeogeogr. Palaeoclimatol. Palaeoecol. 1, 13–37. https://doi.org/10.1016/0031-0182(65)90004-0.
Laskar, J., Robutel, P., Joutel, F., Gastineau, M., Correia, A.C.M., Levrard, B., 2004. A long-term numerical solution for the insolation quantities of the Earth. A&A 428, 261–285. https://doi.org/10.1051/0004-6361:20041335.
Liu, Q., Roberts, A.P., Larrasoaña, J.C., Banerjee, S.K., Guyodo, Y., Tauxe, L., Oldfield, F., 2012. Environmental magnetism: Principles and applications. Rev. Geophys. 50. https://doi.org/10.1029/2012RG000393.
Lückge, A., Doose-Rolinski, H., Khan, A.A., Schulz, H., von Rad, U., 2001. Monsoonal variability in the northeastern Arabian Sea during the past 5000 years: geochemical evidence from laminated sediments. Palaeogeogr. Palaeoclimatol. Palaeoecol. 167, 273–286. https://doi.org/10.1016/S0031-0182(00)00241-8.
Ludwikowska-Kędzia, M., 2000. Ewolucja Srodkowego´Odcinka Doliny Rzeki Belnianki W PoŹnym Glacjale I Holocenie [Evolution of the Middle Segment of the Belnianka River Valley in the Late Glacial and Holocene]. Dialog Press, Warsaw, p. 180.
Lutz, A.F., Immerzeel, W.W., Shrestha, A.B., Bierkens, M.F.P., 2014. Consistent increase in High Asia's runoff due to increasing glacier melt and precipitation. Nat. Clim. Chang. 4, 587–592. https://doi.org/10.1038/nclimate2237.
Maher, B.A., Thompson, R., 1992. Paleoclimatic significance of the mineral magnetic record of the Chinese loess and paleosols. Quat. Res. 37, 155–170. https://doi.org/10.1016/0033-5894(92)90079-X.
McKay, N.P., Emile-Geay, J., Khider, D., 2021. geoChronR – an R package to model, analyze, and visualize age-uncertain data. Geochronology 3, 149–169. https://doi.org/10.5194/gchron-3-149-2021.
Mishra, P.K., Anoop, A., Schettler, G., Prasad, S., Jehangir, A., Menzel, P., Naumann, R., Yousuf, A.R., Basavaiah, N., Deenadayalan, K., Wiesner, M.G., Gaye, B., 2015. Reconstructed late Quaternary hydrological changes from Lake Tso Moriri, NW Himalaya. In: Quaternary International, Updated Quaternary Climatic Research in parts of the Third Pole selected papers from the HOPE-2013 Conference, Nainital, India, vol. 371, pp. 76–86. https://doi.org/10.1016/j.quaint.2014.11.040.
Misra, P., Tandon, S.K., Sinha, R., 2019. Holocene climate records from lake sediments in India: Assessment of coherence across climate zones. Earth Sci. Rev. 190, 370–397. https://doi.org/10.1016/j.earscirev.2018.12.017.
Misra, P., Farooqui, A., Sinha, R., Khanolkar, S., Tandon, S.K., 2020. Millennial-scale vegetation and climatic changes from an early to Mid-Holocene lacustrine archive in Central Ganga Plains using multiple biotic proxies. Quat. Sci. Rev. 243, 106474. https://doi.org/10.1016/j.quascirev.2020.106474.
Murray, M.R., 2002. Is laser particle size determination possible for carbonate-rich lake sediments? J. Paleolimnol. 27, 173–183. https://doi.org/10.1023/A:1014281412035.
Nag, D., Phartiyal, B., Agrawal, S., Kumar, P., Sharma, R., Kumar, K., Sharma, A., Joshi, M., 2023. Westerly-monsoon variations since the last deglaciation from semi-arid Ladakh region, Trans Himalaya, India. Palaeogeogr. Palaeoclimatol. Palaeoecol. 618, 111515. https://doi.org/10.1016/j.palaeo.2023.111515.

Nair, P.J., Chakraborty, A., Varikoden, H., Francis, P.A., Kuttippurath, J., 2018. The local and global climate forcings induced inhomogeneity of Indian rainfall. Sci. Rep. 8, 6026. https://doi.org/10.1038/s41598-018-24021-x.
Neff, U., Burns, S.J., Mangini, A., Mudelsee, M., Fleitmann, D., Matter, A., 2001. Strong coherence between solar variability and the monsoon in Oman between 9 and 6 kyr ago. Nature 411, 290–293. https://doi.org/10.1038/35077048.
North Greenland Ice Core Project members, 2004. High-resolution record of Northern Hemisphere climate extending into the last interglacial period. Nature 431, 147–151. https://doi.org/10.1038/nature02805.
Oldfield, F., 2007. Sources of fine-grained magnetic minerals in sediments: a problem revisited. The Holocene 17, 1265–1271. https://doi.org/10.1177/0959683607085135.
Oldfield, F., Crowther, J., 2007. Establishing fire incidence in temperate soils using magnetic measurements. Palaeogeogr. Palaeoclimatol. Palaeoecol. 249, 362–369. https://doi.org/10.1016/j.palaeo.2007.02.007.
Oldfield, F., Maher, B.A., Donoghue, J., Pierce, J., 1985. Particle-size related, mineral magnetic source sediment linkages in the Rhode River catchment, Maryland, USA. J. Geol. Soc. Lond. 142, 1035–1046. https://doi.org/10.1144/gsjgs.142.6.1035.
Oldfield, F., Battarbee, R.W., Boyle, J.F., Cameron, N.G., Davis, B., Evershed, R.P., McGovern, A.D., Jones, V., Thompson, R., Walker, R., 2010. Terrestrial and aquatic ecosystem responses to late Holocene climate change recorded in the sediments of Lochan Uaine, Cairngorms, Scotland. Quat. Sci. Rev. 29, 1040–1054. https://doi.org/10.1016/j.quascirev.2010.01.007.
Overpeck, J., Anderson, D., Trumbore, S., Prell, W., 1996. The southwest Indian Monsoon over the last 18 000 years. Clim. Dyn. 12, 213–225. https://doi.org/10.1007/BF00211619.
Parnell, A., 2016. Bchron: Radiocarbon Dating, Age-Depth Modelling, Relative Sea Level Rate Estimation, and Non-Parametric Phase Modelling. R Package Version 4.1.1. http://CRAN.R-project.org/package=Bchron.
Passega, R., 1964. Grain size representation by CM patterns as a geologic tool. J. Sediment. Res. 34, 830–847. https://doi.org/10.1306/74D711A4-2B21-11D7-8648000102C1865D.
Paterson, G.A., Heslop, D., 2015. New methods for unmixing sediment grain size data. Geochem. Geophys. Geosyst. 16, 4494–4506. https://doi.org/10.1002/2015GC006070.
Phartiyal, B., Tiwari, A., Kawsar, M., Mc, M., Shekhar, M., Ali, S.N., Bhushan, R., Pachchigar, R.R., Kumar, A., Sharma, A., 2024. Millennial to centennial-scale climate oscillations since 15000 cal yrs BP from Kanwar wetland in the Central Ganga Plain, India. Quat. Sci. Rev. 335, 108760. https://doi.org/10.1016/j.quascirev.2024.108760.
Pokharia, A.K., Sharma, S., Tripathi, D., Mishra, N., Pal, J.N., Vinay, R., Srivastava, A., 2017. Neolithic–early historic (2500–200 BC) plant use: the archaeobotany of Ganga Plain, India. Quat. Int. 443, 223–237. https://doi.org/10.1016/j.quaint.2016.09.018.
Ponton, C., Giosan, L., Eglinton, T.I., Fuller, D.Q., Johnson, J.E., Kumar, P., Collett, T.S., 2012. Holocene aridification of India. Geophys. Res. Lett. 39. https://doi.org/10.1029/2011GL050722.
Prasad, S., Enzel, Y., 2006. Holocene Paleoclimates of India. Quat. Res. 66, 442–453. https://doi.org/10.1016/j.yqres.2006.05.008.
Prasad, S., Kusumgar, S., Gupta, S.K., 1997. A mid to late Holocene record of palaeoclimatic changes from Nal Sarovar: a palaeodesert margin lake in western India. J. Quat. Sci. 12, 153–159. https://doi.org/10.1002/(SICI)1099-1417(199703/04)12:2<153::AID-JQS300>3.0.CO;2-X.
Prasad, V., Phartiyal, B., Sharma, A., 2007. Evidence of enhanced winter precipitation and the prevalence of a cool and dry climate during the mid to late Holocene in mainland Gujarat, India. Holocene 17, 889–896. https://doi.org/10.1177/0959683607082403.
Prasad, S., Anoop, A., Riedel, N., Sarkar, S., Menzel, P., Basavaiah, N., Krishnan, R., Fuller, D., Plessen, B., Gaye, B., Röhl, U., Wilkes, H., Sachse, D., Sawant, R., Wiesner, M.G., Stebich, M., 2014. Prolonged monsoon droughts and links to Indo-Pacific warm pool: a Holocene record from Lonar Lake, Central India. Earth Planet. Sci. Lett. 391, 171–182. https://doi.org/10.1016/j.epsl.2014.01.043.
Prins, M.A., Weltje, G.J., 1999. End-member modeling of siliciclastic grain-size distributions: The late Quaternary record of aeolian and fluvial sediment supply to the Arabian Sea and its paleoclimatic significance. In: Harbaugh, J. (Ed.), Numerical Experiments in Stratigraphy: Recent Advances in Stratigraphic and Sedimentologic Computer Simulations, SEPM Special Publication. Society for Sedimentary Geology, pp. 91–111.
Quamar, M.F., Thakur, B., Sharma, A., Kumar, K., Tiwari, P., Tiwari, A., Prasad, N., Srivastava, J., Phartiyal, B., Manoj, M.C., Roy, I., Saraf, P.N., Prasanna, K., Ali, N., Khan, I., Pandey, S., Trivedi, A., 2024. Multiproxy studies on the spatially distinct surface samples to reconstruct palaeoecology and palaeoclimate from the Core Monsoon Zone of India. J. Palaeontol. Soc. India, 05529360241240095. https://doi.org/10.1177/05529360241240095.
R Core Team, 2019. R: A Language and Environment for Statistical Computing. R Foundation for Statistical Computing, Vienna, Austria. https://www.R-project.org/.
Rasmussen, S.O., Vinther, B.M., Clausen, H.B., Andersen, K.K., 2007. Early Holocene climate oscillations recorded in three Greenland ice cores. Quatern. Sci. Rev. 26, 1907–1914. https://doi.org/10.1016/j.quascirev.2007.06.015.
Rawat, S., Gupta, A.K., Sangode, S.J., Srivastava, P., Nainwal, H.C., 2015. Late Pleistocene–Holocene vegetation and Indian summer monsoon record from the Lahaul, Northwest Himalaya, India. Quat. Sci. Rev. 114, 167–181. https://doi.org/10.1016/j.quascirev.2015.01.032.
Rawat, V., Rawat, S., Srivastava, P., Negi, P.S., Prakasam, M., Kotlia, B.S., 2021. Middle Holocene Indian summer monsoon variability and its impact on cultural changes in the Indian subcontinent. Quat. Sci. Rev. 255, 106825. https://doi.org/10.1016/j.quascirev.2021.106825.
Reimer, P.J., Austin, W.E., Bard, E., Bayliss, A., Blackwell, P.G., Ramsey, C.B., Butzin, M., Cheng, H., Edwards, R.L., Friedrich, M., Grootes, P.M., 2020. The IntCal20 Northern Hemisphere radiocarbon age calibration curve (0–55 cal kBP). Radiocarbon 62, 725–757.
Resmi, M.R., Achyuthan, H., Deopa, H., 2022. Holocene Monsoonal Variations over Southern India: looking into its Antecedents. Front. Earth Sci. 9. https://doi.org/10.3389/feart.2021.717420.
Roberts, A.P., 1995. Magnetic properties of sedimentary greigite (Fe3S4). Earth Planet. Sci. Lett. 134, 227–236. https://doi.org/10.1016/0012-821X(95)00131-U.
Roxy, M., Patil, N., Aparna, K., Ashok, K., 2013. Revisiting the Indian summer monsoon–ENSO links in the IPCC AR4 projections: a cautionary outlook. Glob. Planet. Chang. 104, 51–60. https://doi.org/10.1016/j.gloplacha.2013.02.003.
Sabeerali, C.T., Ajayamohan, R.S., Bangalath, H.K., Chen, N., 2019. Atlantic zonal mode: an emerging source of Indian summer monsoon variability in a warming world. Geophys. Res. Lett. 46, 4460–4467. https://doi.org/10.1029/2019GL082379.
Saji, N.H., Goswami, B.N., Vinayachandran, P.N., Yamagata, T., 1999. A dipole mode in the tropical Indian Ocean. Nature 401, 360–363. https://doi.org/10.1038/43854.
Sandeep, K., Warrier, A.K., Harshavardhana, B.G., Shankar, R., 2012. Rock magnetic investigations of surface and sub-surface soil samples from five lake catchments in tropical Southern India. Int. J. Environ. Res. 6, 1–18. https://doi.org/10.22059/ijer.2011.467.
Sandeep, K., Shankar, R., Warrier, A.K., Yadava, M.G., Ramesh, R., Jani, R.A., Weijian, Z., Xuefeng, L., 2017. A multi-proxy lake sediment record of Indian summer monsoon variability during the Holocene in southern India. Palaeogeogr. Palaeoclimatol. Palaeoecol. 476, 1–14. https://doi.org/10.1016/j.palaeo.2017.03.021.
Saraswat, R., Naik, D.K., Nigam, R., Gaur, A.S., 2016. Timing, cause and consequences of mid-Holocene climate transition in the Arabian Sea. Quat. Res. 86, 162–169. https://doi.org/10.1016/j.yqres.2016.06.001.
Sarkar, S., Prasad, S., Wilkes, H., Riedel, N., Stebich, M., Basavaiah, N., Sachse, D., 2015. Monsoon source shifts during the drying mid-Holocene: Biomarker isotope based evidence from the core 'monsoon zone' (CMZ) of India. Quat. Sci. Rev. 123, 144–157. https://doi.org/10.1016/j.quascirev.2015.06.020.
Saxena, A., Singh, D.S., 2017. Multiproxy records of vegetation and monsoon variability from the lacustrine sediments of eastern Ganga Plain since 1350 A.D. Quat. Int. 444, 24–34. https://doi.org/10.1016/j.quaint.2016.08.003.
Saxena, A., Trivedi, A., 2017. Pollen based vegetation and climate change records deduced from the lacustrine sediments of Kikar Tal (Lake), Central Ganga Plain, India. J. Palaeosci. 66, 37–46. https://doi.org/10.54991/jop.2017.278.
Saxena, A., Singh, I.B., Agarwal, P.N., 2011. Palaeoecological implication of ostracod and gastropod assemblages of the Holocene lake records from the Ganga Plain. J. Palaeontol. Soc. India 56, 149–163. https://doi.org/10.1177/0971102320110204.
Saxena, A., Prasad, V., Singh, I.B., 2013. Holocene palaeoclimate reconstruction from the phytoliths of the lake-fill sequence of Ganga Plain. Curr. Sci. 104, 1054–1062.
Saxena, A., Trivedi, A., Chauhan, M.S., Sharma, A., 2015. Holocene vegetation and climate change in Central Ganga Plain: a study based on multiproxy records from Chaudhary-Ka-Tal, Raebareli District, Uttar Pradesh, India. Quat. Int. 371, 164–174. https://doi.org/10.1016/j.quaint.2015.01.041.
Scholz, C.A., Johnson, T.C., Cohen, A.S., King, J.W., Peck, J.A., Overpeck, J.T., Talbot, M. R., Brown, E.T., Kalindekafe, L., Amoako, P.Y.O., Lyons, R.P., Shanahan, T.M., Castañeda, I.S., Heil, C.W., Forman, S.L., McHargue, L.R., Beuning, K.R., Gomez, J., Pierson, J., 2007. East African megadroughts between 135 and 75 thousand years ago and bearing on early-modern human origins. Proc. Natl. Acad. Sci. 104, 16416–16421. https://doi.org/10.1073/pnas.0703874104.
Sengupta, S., Gupta, A.K., Jaiswal, M.K., Kumar, P., Sanyal, P., Pandey, S., Sen Singh, D., Kaushik, A., Singh, A.K., Palar, B., Sharma, R., Singh, V., 2024. Palaeoclimatic shifts in the Central Ganga Basin during the Middle- to late Holocene: Exploring the 4.2 ka arid event and its implications in northern India. The Holocene, 09596836241247310. https://doi.org/10.1177/09596836241247310.
Sharma, S., Joachimski, M., Sharma, M., Tobschall, H.J., Singh, I.B., Sharma, C., Chauhan, M.S., Morgenroth, G., 2004. Lateglacial and Holocene environmental changes in Ganga plain, Northern India. Quat. Sci. Rev. 23, 145–159. https://doi.org/10.1016/j.quascirev.2003.10.005.
Sharma, R., Umapathy, G.R., Kumar, P., Ojha, S., Gargari, S., Joshi, R., Chopra, S., Kanjilal, D., 2019. AMS and upcoming geochronology facility at Inter University Accelerator Centre (IUAC), New Delhi, India. Nucl. Instrum. Methods Phys. Res., Sect. B 438, 124–130. https://doi.org/10.1016/j.nimb.2018.07.002.
Shindell, D.T., Schmidt, G.A., Mann, M.E., Rind, D., Waple, A., 2001. Solar forcing of regional climate change during the Maunder Minimum. Science. 294, 2149–2152. https://doi.org/10.1126/science.1064363.
Singh, I.B., 1996. Geological evolution of Ganga Plain: an overview. J. Palaeontol. Soc. India. 41, 99–137.
Singh, I.B., 2005. Climate change and human history in Ganga Plain during late Pleistocene-Holocene. J. Palaeosci. 54, 1–12. https://doi.org/10.54991/jop.2005.67.
Singh, I.B., Rajagopalan, G., Agarwal, K.K., Srivastava, P., Sharma, M., Sharma, S., 1997. Evidence of middle to late Holocene neotectonic activity in the Ganga Plain. Curr. Sci. 73, 1114–1117.
Singh, D.S., Gupta, A.K., Sangode, S.J., Clemens, S.C., Prakasam, M., Srivastava, P., Prajapati, S.K., 2015. Multiproxy record of monsoon variability from the Ganga Plain during 400–1200 a.D. Quat. Int. 371, 157–163. https://doi.org/10.1016/j.quaint.2015.02.040.

Singh, S., Gupta, A.K., Rawat, S., Bhaumik, A.K., Kumar, P., Rai, S.K., 2022. Paleomonsoonal shifts during ~13700 to 3100 yr BP in the central Ganga Basin, India with a severe arid phase at ~4.2 ka. Quat. Int. 629, 65–73. https://doi.org/10.1016/j.quaint.2021.01.015.

Sinha, R., Tandon, S., Gibling, M., Bhattacharjee, P., Dasgupta, A.S., 2005. Late Quaternary geology and alluvial stratigraphy of the Ganga basin. Himal. Geol. 26, 223–240.

Sinha, R., Smykatz-Kloss, W., Stüben, D., Harrison, S.P., Berner, Z., Kramar, U., 2006. Late Quaternary palaeoclimatic reconstruction from the lacustrine sediments of the Sambhar playa core, Thar Desert margin, India. Palaeogeogr. Palaeoclimatol. Palaeoecol. 233, 252–270. https://doi.org/10.1016/j.palaeo.2005.09.012.

Sinha, A., Cannariato, K.G., Stott, L.D., Cheng, H., Edwards, R.L., Yadava, M.G., Ramesh, R., Singh, I.B., 2007. A 900-year (600 to 1500 a.D.) record of the Indian summer monsoon precipitation from the core monsoon zone of India. Geophys. Res. Lett. 34. https://doi.org/10.1029/2007GL030431.

Sinha, A., Stott, L., Berkelhammer, M., Cheng, H., Edwards, R.L., Buckley, B., Aldenderfer, M., Mudelsee, M., 2011. A global context for megadroughts in monsoon Asia during the past millennium. Quat. Sci. Rev. 30, 47–62. https://doi.org/10.1016/j.quascirev.2010.10.005.

Sinha, N., Gandhi, N., Chakraborty, S., Krishnan, R., Yadava, M., Ramesh, R., 2018. Abrupt climate change at ~2800 yr BP evidenced by a stalagmite record from peninsular India. Holocene 28 (11), 1720–1730. https://doi.org/10.1177/0959683618788647.

Sirocko, F., Sarnthein, M., Lange, H., Erlenkeuser, H., 1991. Atmospheric summer circulation and coastal upwelling in the Arabian Sea during the Holocene and the last glaciation. Quat. Res. 36, 72–93. https://doi.org/10.1016/0033-5894(91)90018-Z.

Sirocko, F., Garbe-Schonberg, D., McIntyre, A., Molfino, B., 1996. Teleconnections between the subtropical monsoons and high-latitude climates during the last deglaciation. Science 272, 526–529.

Snowball, I.F., 1991. Magnetic hysteresis properties of greigite (Fe3S4) and a new occurrence in Holocene sediments from Swedish Lappland. Phys. Earth Planet. Inter. 68, 32–40. https://doi.org/10.1016/0031-9201(91)90004-2.

Snowball, I.F., 1994. Bacterial magnetite and the magnetic properties of sediments in a Swedish lake. Earth Planet. Sci. Lett. 126, 129–142. https://doi.org/10.1016/0012-821X(94)90246-1.

Snowball, I., Thompson, R., 1990. A mineral magnetic study of Holocene sedimentation in Lough Catherine, Northern Ireland. Boreas 19, 127–146. https://doi.org/10.1111/j.1502-3885.1990.tb00574.x.

Srivastava, P., Singh, I.B., Sharma, M., Singhvi, A.K., 2003a. Luminescence chronometry and late Quaternary geomorphic history of the Ganga Plain, India. Palaeogeogr. Palaeoclimatol. Palaeoecol. 197, 15–41. https://doi.org/10.1016/S0031-0182(03)00384-5.

Srivastava, P., Singh, I.B., Sharma, S., Shukla, U.K., Singhvi, A.K., 2003b. Late Pleistocene–Holocene hydrologic changes in the interfluve areas of the central Ganga Plain, India. Geomorphology 54, 279–292. https://doi.org/10.1016/S0169-555X(02)00361-6.

Srivastava, P., Agnihotri, R., Sharma, D., Meena, N., Sundriyal, Y.P., Saxena, A., Bhushan, R., Sawlani, R., Banerji, U.S., Sharma, C., Bisht, P., Rana, N., Jayangondaperumal, R., 2017. 8000-year monsoonal record from Himalaya revealing reinforcement of tropical and global climate systems since mid-Holocene. Sci. Rep. 7, 14515. https://doi.org/10.1038/s41598-017-15143-9.

Staubwasser, M., Sirocko, F., Grootes, P.M., Erlenkeuser, H., 2002. South Asian monsoon climate change and radiocarbon in the Arabian Sea during early and middle Holocene. Paleoceanography 17, 15-1-15-12. https://doi.org/10.1029/2000PA000608.

Sukumar, R., Ramesh, R., Pant, R.K., Rajagopalan, G., 1993. A δ13C record of late Quaternary climate change from tropical peats in southern India. Nature 364, 703–706. https://doi.org/10.1038/364703a0.

Sun, B., Li, H., Zhou, B., 2019. Interdecadal variation of Indian Ocean basin mode and the impact on Asian summer climate. Geophys. Res. Lett. 46, 12388–12397. https://doi.org/10.1029/2019GL085019.

Tewari, R., Hemraj, Srivastava, R.K., 1996. Excavations at Hulaskhera, Lucknow, 1978-79 to 1986-87. Pragdhara 6, 95–133.

Thamban, M., Kawahata, H., Rao, V.P., 2007. Indian summer monsoon variability during the holocene as recorded in sediments of the Arabian Sea: timing and implications. J. Oceanogr. 63, 1009–1020. https://doi.org/10.1007/s10872-007-0084-8.

Thompson, R., Oldfield, F., 1986. Mineral magnetism in marine sediments. In: Thompson, R., Oldfield, F. (Eds.), Environmental Magnetism. Springer Netherlands, Dordrecht, pp. 141–152. https://doi.org/10.1007/978-94-011-8036-8_12.

Trenberth, K.E., Shea, D.J., 2005. Relationships between precipitation and surface temperature. Geophys. Res. Lett. 32. https://doi.org/10.1029/2005GL022760.

Tripathi, D., Chauhan, D.K., Farooqui, A., Kotlia, B.S., Thakur, B., Morthekai, P., Long, T., Chauhan, M.S., Pokharia, A.K., 2017. Late Quaternary climatic variability in the Central Ganga Plain: a multi-proxy record from Karela Jheel (Lake). Quat. Int. 443, 70–85. https://doi.org/10.1016/j.quaint.2016.11.033.

Trivedi, A., Chauhan, M.S., Sharma, A., Nautiyal, C.M., Tiwari, D.P., 2013. Record of vegetation and climate during Late Pleistocene–Holocene in Central Ganga Plain, based on multiproxy data from Jalesar Lake, Uttar Pradesh, India. Quat. Int. 306, 97–106. https://doi.org/10.1016/j.quaint.2013.04.010.

Trivedi, A., Saxena, A., Chauhan, M.S., Sharma, A., Farooqui, A., Nautiyal, C.M., Yao, Y.-F., Wang, Y.-F., Li, C.-S., Tiwari, D.P., 2019. Vegetation, climate and culture in Central Ganga plain, India: a multi-proxy record for Last Glacial Maximum. Quat. Int. 507, 134–147. https://doi.org/10.1016/j.quaint.2019.02.019.

Trivedi, A., Agrawal, S., Sharma, A., Ali, S.N., Manoj, M.C., Nag, A., Misra, S., Kawsar, M., 2024. Climatic Oscillations and Dynastic Trends: a Multiproxy analysis of the past two millennia in the Indian Subcontinent. CATENA 246, 108424. https://doi.org/10.1016/j.catena.2024.108424.

Vaasma, T., 2008. Grain-size analysis of lacustrine sediments: a comparison of pre-treatment methods. Estonian J. Ecol. 57, 231. https://doi.org/10.3176/eco.2008.4.01.

Vali, H., Förster, O., Amarantidis, G., Petersen, N., 1987. Magnetotactic bacteria and their magnetofossils in sediments. Earth Planet. Sci. Lett. 86, 389–400. https://doi.org/10.1016/0012-821X(87)90235-4.

van Hateren, J.A., Prins, M.A., van Balen, R.T., 2018. On the genetically meaningful decomposition of grain-size distributions: a comparison of different end-member modelling algorithms. Sediment. Geol. Anal. Sediment Properties 375, 49–71. https://doi.org/10.1016/j.sedgeo.2017.12.003.

Walden, J.F., Oldfield, F., Smith, J., 1999. Environmental Magnetism: A Practical Guide, no.6. Quaternary Research Association, London.

Walter, H., Lieth, H., 1967. Klimadiagram – Weltatlas. VEB Gautav Fischer Verlage, Jena.

Wang, Y., Cheng, H., Edwards, R.L., He, Y., Kong, X., An, Z., Wu, J., Kelly, M.J., Dykoski, C.A., Li, X., 2005. The Holocene Asian Monsoon: links to solar changes and north Atlantic climate. Science 308, 854–857. https://doi.org/10.1126/science.1106296.

Wanner, H., Mercolli, L., Grosjean, M., Ritz, S.P., 2015. Holocene climate variability and change; a data-based review. JGS 172, 254–263. https://doi.org/10.1144/jgs2013-101.

Warrier, A.K., Mahesh, B.S., Mohan, R., Shankar, R., Asthana, R., Ravindra, R., 2014. Glacial–interglacial climatic variations at the Schirmacher Oasis, East Antarctica: the first report from environmental magnetism. Palaeogeogr. Palaeoclimatol. Palaeoecol. 412, 249–260. https://doi.org/10.1016/j.palaeo.2014.08.007.

Wentworth, C.K., 1922. A scale of grade and class terms for clastic sediments. J. Geol. 30, 377–392.

Wünnemann, B., Demske, D., Tarasov, P., Kotlia, B.S., Reinhardt, C., Bloemendal, J., Diekmann, B., Hartmann, K., Krois, J., Riedel, F., Arya, N., 2010. Hydrological evolution during the last 15 kyr in the Tso Kar lake basin (Ladakh, India), derived from geomorphological, sedimentological and palynological records. Quat. Sci. Rev. 29, 1138–1155. https://doi.org/10.1016/j.quascirev.2010.02.017.

Zepner, L., Karrasch, P., Wiemann, F., Bernard, L., 2021. ClimateCharts.net – an interactive climate analysis web platform. Int. J. Dig. Earth 14, 338–356. https://doi.org/10.1080/17538947.2020.1829112.